

Manuscript prepared for J. Name
with version 2014/09/16 7.15 Copernicus papers of the L^AT_EX class coperni-
cus.cls.
Date: 22 August 2022

This document is the accepted manuscript version of the following article:
Corbin, J. C., Modini, R. L., & Gysel-Beer, M. (2022). Mechanisms of soot-aggregate
restructuring and compaction. *Aerosol Science and Technology*.
<https://doi.org/10.1080/02786826.2022.2137385>

Mechanisms of soot-aggregate restructuring and compaction

Joel C. Corbin^{1,2}, Robin L. Modini¹, and Martin Gysel-Beer¹

¹Laboratory of Atmospheric Chemistry, Paul Scherrer Institute, 5232 Villigen, Switzerland

²Now at: Metrology Research Centre, National Research Council Canada, 1200 Montreal Rd, Ottawa, Canada

Correspondence to: Joel.Corbin@nrc-cnrc.gc.ca

Abstract.

Soot aggregates form as open, fractal-like structures, but aged atmospheric particles are often observed to be restructured into more-compact shapes due to internal mixing (“coating”). This compaction has a major effect on the radiative properties of the aggregates, and may also influence their aerosol-cloud interactions, toxicity, and deposition in human lungs. Recent laboratory studies have presented conflicting arguments on whether this compaction occurs during condensation or during the evaporation of coatings. In this three-part study, we combine theory and experiments to explain these conflicting results. First, we review the surface-science literature and identify explicit mechanisms for condensation-compaction as well as evaporation-compaction. We also identify a mechanism for *avoiding* compaction during condensation, based on heterogeneous nucleation theory and the kinetic barriers to capillary formation. Second, we review the soot-restructuring literature and find clear evidence for both condensation- and evaporation-compaction, with condensation-compaction being the norm. Third, we present new experimental results where the capillary forces due to anthracene coatings were “switched on” or “switched off” by using solid or liquid phases during coating addition and removal. Consequently, we demonstrate condensation-compaction, evaporation-compaction, and no compaction, for the same soot source. Overall, our study indicates that soot particles will typically undergo compaction when internal mixing occurs by the condensation of liquid coatings, while compaction may be avoided when internal mixing occurs through coagulation or the gas-to-particle formation of solid or highly viscous coatings.

1 Introduction

Globally, soot particles are predicted to absorb comparable amounts of solar radiation as carbon dioxide, with the exact absorption amount depending on the concentration of soot particles and their mixing with other particulate material (PM) (Ramanathan and Carmichael, 2008; Bond *et al.*, 2013). However, describing the radiative properties of soot BC as a function of atmospheric lifetime remains a major challenge (Cappa *et al.*, 2012; Jacobson, 2013; Cappa *et al.*, 2013) due to variability in the morphologies of the BC spherules which comprise soot (Yon *et al.*, 2014; Radney *et al.*, 2014) and the various possible configurations of soot with other internally-mixed material (Adachi *et al.*, 2010; Liu and Mishchenko, 2018). A key issue is whether the spherules comprising soot aggregates are arranged in extremely open, fractal-like structures (Eggersdorfer and Pratsinis, 2013) or more compact, spheroidal shapes (Zangmeister *et al.*, 2014). This change of structure strongly influences their optical properties (Qiu *et al.*, 2012; Scarnato *et al.*, 2013; Radney *et al.*, 2014; Hu *et al.*, 2022; Kelesidis *et al.*, 2022).

The open and compact limits of soot spherule morphology are defined by the normally distinct processes of aggregate formation and of internal mixing. Soot aggregates, like other flame-synthesized aggregates, are formed by the diffusion-limited clustering of spherules (Eggersdorfer and Pratsinis, 2013) with diameters roughly 10–80 nm spherules (Corbin *et al.*, 2019), which produces open-structured aggregates (Eggersdorfer and Pratsinis, 2013) as observed at or near combustion source. However, electron microscopy of atmospherically aged soot often shows these spherules to be highly compacted (Xiong and Friedlander, 2001; Abel *et al.*, 2003; Shi *et al.*, 2003; Johnson *et al.*, 2005; Niemi *et al.*, 2006; Adachi and Buseck, 2008; Worringen *et al.*, 2008; Adachi *et al.*, 2010; Coz and Leck, 2011; Adachi and Buseck, 2013; China *et al.*, 2014, 2015b; Bhandari *et al.*, 2019), apparently due to internal mixing with non-refractory material (often referred to as “coating”, whether occurring due to condensation or coagulation).

Historically, it has been widely believed that soot particles were compacted by capillary forces upon the condensation of coatings (Kütz and Schmidt-Ott, 1992; Zhang *et al.*, 2008; Qiu *et al.*, 2012; Khalizov *et al.*, 2013). This belief generally relied on indirect evidence, due to the difficulty of measuring the structure of a soot particle while it remains coated. In contrast to this common belief, Ma *et al.* (2013a) directly observed that soot particles could remain open in structure after coating by water. The same particles were compacted after evaporation of the water coating. In the Ma *et al.* (2013a) experiments, restructuring therefore occurred during evaporation, not condensation. Although Ma *et al.* (2013a) did not recommend that their observations should be extrapolated to all atmospheric and combustion systems, many authors have since begun to model coated soot particles as open in structure (Dong *et al.*, 2015; Heinson *et al.*, 2016; Wu *et al.*, 2016, 2017; Wang *et al.*, 2017; Luo *et al.*, 2018; Liu *et al.*, 2016; Lefevre *et al.*, 2019; Luo *et al.*, 2021; Zheng and Wu, 2021; Romshoo *et al.*, 2021). Other authors still model restructuring as occurring upon condensation, in both numerical work (Fierce *et al.*, 2016; Wu *et al.*, 2017; Luo *et al.*, 2018; Kahnert, 2017; Kanngießner and Kahnert, 2018; Luo *et al.*, 2020) and the interpretation of measurements (Cappa *et al.*, 2012; Rissler *et al.*, 2013; Peng *et al.*, 2016; Zhang *et al.*, 2018; Cappa *et al.*, 2019; Fierce *et al.*, 2020; Yuan *et al.*, 2021; Hu *et al.*, 2022; Gao *et al.*, 2022). Meanwhile, subtle but clear experimental evidence that condensation does lead to soot restructuring has not been fully acknowledged (Section 3 of this work).

The morphology of soot aggregates influences their light absorption and physical properties, as relevant to climate, health impacts and other contexts. Fractal-like soot aggregates scatter up to 30 % more light (Scarnato *et al.*, 2013; Radney *et al.*, 2014), and the optical properties of a coated soot particle which remains open in morphology are significantly different from a compacted one (Scarnato *et al.*, 2013; Kelesidis *et al.*, 2022). Experimentally, the relative absorption enhancement caused by coatings on soot is often measured by comparing the absorption properties of coated and denuded soot (Cappa *et al.*, 2012; Lack *et al.*, 2012); this comparison would be biased if the denuded soot was compacted but the coated soot was not. In terms of health impacts, fractal-like aggregates may deposit in the human lung at a different rate than compacted ones (Scheckman and McMurphy, 2011; Rissler *et al.*, 2012). The humid environment of the human lungs may potentially trigger compaction for hygroscopic soot particles, influencing their size and surface area, and therefore their health impacts. In a 1975 study, Chamberlain *et al.* (1975) directly observed the compaction of soot aggregates after inhalation and exhalation of engine exhaust by human volunteers. Yet Brauer *et al.* (2001) reported two examples of fractal-like soot found in the lungs of lifetime residents of Mexico City during autopsy. In addition, scrubbers used in exhaust aftertreatment have been observed to cause soot restructuring (Lieke *et al.*, 2013); understanding this behaviour would inform engine aftertreatment system design. Finally, the restructuring of synthetic nanoparticle aggregates is a useful procedure in materials science (Kelesidis *et al.*, 2018).

Overall, there is a strong need to progress towards consensus on the causes and mechanisms of soot-aggregate restructuring, as well as to provide a conceptual framework from which the morphological effects of atmospheric aging, cloud processing and human respiration may be predicted. The contribution of the present manuscript towards this goal are to (1) synthesize literature from nucleation, surface and capillary science to identify explicit restructuring mechanisms, based on the processes of phase nucleation, capillary condensation, and droplet formation, (2) critically review the available literature on soot aggregate restructuring for evidence of these four modes, (3) present new experiments designed to resolve some of the conflicts in the literature, using solid or liquid anthracene coatings, and liquid oleic acid.

2 Review of physical mechanisms required for compaction

Aggregate compaction by condensation must proceed via the (i) nucleation and (ii) growth of a liquid phase, resulting in (iii) the torquing of aggregate monomers due to attractive capillary forces caused by surface tension. These 3 steps have not previously been discussed in the context of the literature on phase nucleation, capillary condensation, and droplet formation. We critically review this literature in the present section. Our review provides a basis for the understanding and classification of the experimental studies on aggregate restructuring reviewed in Section 3.

2.1 Nucleation and growth of the liquid phase

Bulk, pure liquid phases may grow when the vapour pressure, p , exceeds the equilibrium vapour pressure over a flat surface, p_0 , at a saturation ratio $S = p/p_0$. Bulk liquid surfaces may grow at S slightly greater than 1, while droplets require $S > 1$ due to their positive curvature (Lamb and Verlinde, 2011). In contrast, nanoscopic quantities of liquid may condense when $S \ll 1$ via the processes discussed in this section. The formation of these nanoscopic phases is generally limited by energy barriers. These energy barriers are important to the process of soot compaction, because they lead to different condensation pathways occurring under different physical conditions. We therefore begin our discussion from the perspective of these barriers.

Liquid condensation onto insoluble surfaces is generally initiated by the nucleation of molecular clusters onto active sites on the surface to form small patches of liquid (Laaksonen, 2015; Laaksonen *et al.*, 2020). These small patches have been observed using atomic force microscopy for both high (Cao *et al.*, 2011) and low (Xu *et al.*, 2010) contact angles, and we refer to them collectively as *nanodroplets*.

If the areal density of nanodroplets formed on an insoluble particle is high enough, the nanodroplets may coalesce to form a *film* (Laaksonen *et al.*, 2020); the required density is lower at lower contact angles. If a film forms between two nearby surfaces (e.g. of two touching soot spherules), then fluctuations in the film–air interface may lead to the sudden coalescence of a *capillary phase* (Crassous *et al.*, 1994; Restagno *et al.*, 2000). The lifetime of the metastable film phase is the capillary-formation timescale, and can be extremely long, as evidenced by the hours required for equilibrium in pore adsorption processes (Bocquet *et al.*, 1998; Restagno *et al.*, 2000; Ferry *et al.*, 2002). However, this lifetime decreases exponentially with increasing temperature (Restagno *et al.*, 2000). Once formed, the capillary phase grows slightly more slowly than if it were diffusion limited (Kohonen *et al.*, 1999).

At a critical point, $S_{\text{crit}} > 1$, nanodroplets, films and capillaries may *activate* into droplets and grow without any remaining energy barriers. This droplet activation may proceed via *nanodroplet activation (NDA)*, *film activation*, or *capillary activation* (Laaksonen *et al.*, 2020). The majority of vapour or “coating” volume will condense at this stage. Crucially, activation may occur before the equilibration of capillary phases, due to the abovementioned long capillary-equilibration timescales.

We note that nucleating substances are often observed to be liquid rather than solid, even below the macroscopic melting point. This phenomenon is attributable to the lower free energy of a liquid-solid interface versus a solid-solid interface (Christenson, 2001) as well as the fact that interfacial energy leads to a melting point depression for nanoscopic quantities of matter, as discussed below.

In summary, depending on the nucleation rate and growth rate of the respective phases (which themselves depend on the liquid–particle contact angle, density of active sites, and temperature), vapour may condense onto soot particles at $S < 1$ as nanodroplets, films, or capillaries. At $S > 1$, activation of these nanodroplets, films, or capillaries into droplets may result in different shapes of metastable liquid phases. These liquid phases may exert unbalanced capillary forces on soot particles, as described in the next subsection.

2.2 Mechanisms of soot compaction during condensation

During the condensational growth of capillaries at $S < 1$ or droplets at $S_{\text{crit}} > 1$, the liquid phase may exert capillary forces on the soot monomers and cause restructuring of the aggregate. These forces will generally be attractive, and must be asymmetric about the point of contact between spherules for compaction to occur. In general, spherule movements due to capillary forces are expected to be extremely rapid ($\ll 1$ second; Narhe and Beysens 2006) relative to the rate of condensation, so we do not focus our discussion on timescales in this section. Rather, we discuss specific mechanisms of condensation-induced compaction, focussing on mechanisms for which direct experimental evidence exists in the literature. All three of the following mechanisms rely on capillary condensates and capillary forces, and we therefore refer to them collectively as *capillary compaction* (CC) mechanisms.

The first and second mechanisms we identify are related to the formation of capillary menisci between two soot spherules (Butt and Kappl, 2009). They both may occur at the step labelled “capillary formation” in Figure 1a. The first CC mechanism occurs during the initial formation of a capillary condensate, when the capillary suddenly forms from the connection of neighbouring films (Section 2.1). This initial connection generates a force about two orders of magnitude larger than the equilibrium capillary force (Crassous *et al.*, 1994) and is therefore not well described by equilibrium-force considerations (Butt and Kappl, 2009).

The second CC mechanism occurs during the growth of capillary phases and films. This growth is accompanied by an advancing liquid-solid-gas interface: the *contact line*. During condensation, this contact line may advance more quickly in one region of the surface than another due to physical heterogeneities on the soot surface, such as variations in curvature, atomic-scale discontinuities or bumps in the graphitic nanostructure (Toth *et al.*, 2019) or chemical heterogeneities due to surface functional groups (Figueiredo *et al.*, 1999; Matuschek *et al.*, 2007; Corbin *et al.*, 2015). These heterogeneities mean that the equilibrium contact angle θ will vary across the soot spherule surface (Gao and McCarthy, 2006), and may also lead to contact line pinning (Fadeev and McCarthy, 1999; Gao and McCarthy, 2006). Pinned contact lines grow via small “jumps” or molecular avalanches (Schäffer and Wong, 2000), which may cause sudden changes and asymmetric torque on the touching spherules.

The effects of pinned contact lines and heterogeneous contact angles on capillary forces can be illustrated by considering the growth of the capillary phase. After the capillary phase forms from the coalescence of nearby films, it may grow until reaching its equilibrium shape: a pendular ring (Butt and Kappl, 2009). (Figure 1a illustrates the cross-section of an imperfect pendular ring at the label “capillary formation”.) During the growth of a pendular ring, both pinned contact lines and heterogeneous contact angles would lead to a greater capillary attraction on one side of the pendular ring than the other, resulting in torque on the touching spherules. This mechanism may also be relevant if a partial pendular ring forms between film coalescence and the formation of a pendular ring. In the real world, asymmetric pendular rings are likely the norm. Even in controlled laboratory studies using polished ruby spheres, Pitois *et al.* (2000) only achieved perfect pendular rings after several cycles of capillary formation. We note that this second CC mechanism is dependent on the rate of capillary growth (Eral *et al.*, 2012; Shi *et al.*, 2018) as well as whether or not the touching spherules are already in motion. Our first and second CC mechanisms are consistent with an earlier, apparently intuitive, suggestion by Kütz and Schmidt-Ott (1992) which was modelled by Schnitzler *et al.* (2017).

A third CC mechanism was also modelled by Schnitzler *et al.* (2017). In this mechanism, two non-neighbouring soot spherules were connected by a capillary phase, which led to an attractive force. While we did not find direct evidence for this *bridge-capillary compaction* mechanism in the literature, such a phase could potentially form if NDA occurs on two different spherules and the activated droplets subsequently coalesce. Alternatively, a capillary bridge could form when pendular capillary rings or adsorbed films grow to engulf the particles which they connect, creating an attractive capillary force between three neighbouring spheres. This engulfment mechanism was explored theoretically by Crouzet and Marlow (1995) for a pair of spheres. The only experimental evidence we have identified for this engulfment hypothesis is provided by the two-dimensional analogy observed directly by Narhe and Beysens (2004). Overall, the only experimental evidence we have identified for bridge-capillary compaction is that of the soot-restructuring study by Chen *et al.* (2018, discussed in Section 3.2.3). Both of these capillary-bridge mechanisms would occur during the step labelled “droplet activation” in Figure 1a.

We have proposed that bridge-capillary compaction may proceed after droplets nucleate by NDA on two (or more) spherules. This would require extremely high supersaturations, to overcome the energy barriers to activation simultaneously for multiple nanodroplets. At less extreme supersaturations, NDA would proceed via the activation of one nanodroplet per aggregate. In this scenario, contact between the growing liquid phase and the soot monomers is minimal, and there is no opportunity for capillary forces to act. Therefore, soot particles coated by NDA are unlikely to be compacted (Figure 1b). This conclusion also extends to the scenario of coating by coagulation, which is discussed further in Section 3.5.6 and Section 5.

Overall, our framework contrasts with the alternative framework proposed by Chen *et al.* (2018), which focussed on the competition between condensational growth rates on curved surfaces versus capillaries. This competition may come into play in some scenarios, though it is less likely to be crucial during atmospheric aging, and does not cover all literature cases reviewed below. In our framework, condensation is limited by the energy barriers to phase formation, not by condensation rates.

2.3 Mechanisms of soot compaction during evaporation

The restructuring of a coated aggregate upon evaporation of a liquid coating (*droplet-evaporation compaction*, DEC) occurs due to the attachment of the liquid surface to the aggregate. From the perspective of a single spherule, this scenario is analogous to that of an isolated particle at a liquid–gas interface, for which the theory is well developed (Butt *et al.*, 2003, p. 123). Compared to condensation compaction, the situation is much simpler because it does not involve the nucleation of a new phase.

At equilibrium, such an isolated spherule would be freely floating in the liquid phase due to the balance of buoyant and surface forces. For contact angles $\theta > 0$, a small “cap” defined by the contact angle will protrude from the liquid interface (Ref. 229 in Butt *et al.*, 2003). During the evaporation of a relatively large droplet, the isolated spherule would be pulled inwards by the capillary force of the retreating liquid–air interface. If the spherule was part of an aggregate, this retreating interface would eventually come into contact with two or more spherules. At this critical point, two or more spherules would be pulled inwards, and the aggregate would begin to experience a net compacting force, causing *evaporation-compaction* (Figure 1c). This has been exploited in materials science (Manoharan, 2003; Lauga and Brenner, 2004). For contact angles $> 90^\circ$, this force is still present (Lauga and Brenner, 2004); the only effect of the high contact angle is that more than half of the spherule area moves to the gas interface (Butt *et al.*, 2003) (in a bulk liquid, the spherule would appear to float higher).

For evaporation-compaction to be the dominant restructuring mechanism, the soot aggregate must first be incorporated into a droplet without undergoing substantial compaction. We discuss scenarios for this in Section 3.

3 Review of experimental demonstrations of aggregate restructuring mechanisms

Dozens of studies have either focussed on or commented on the restructuring of soot after exposure to condensable vapours. In this section, we review these studies in light of the restructuring mechanisms identified above and summarized in Figure 1. For completeness, we also include here those relatively few studies which have investigated the restructuring of aerosol aggregates or agglomerates other than soot. We find that the literature is consistent with the identified mechanisms, with no exceptions that are relevant to atmospheric science. For completeness, we also discuss here those exceptions and some related topics.

3.1 Background: electron microscopy, mobility size, and shape factor

Before reviewing the literature in earnest, we briefly introduce two of the most common techniques for compaction measurements. The first technique, electron microscopy, is invaluable, but requires low-pressure conditions (vacuum or near vacuum) for analysis, which triggers the evaporation of volatile coatings. The electron beam itself may also trigger evaporation, which hinders the imaging of coated soot aggregates. Additionally, the labour intensive nature of microscopy means that such studies typically report measurements on tens or hundreds of particles, rather than the orders of magnitude more measured by the second common technique.

The second common technique, mobility diameter d_{mob} measurements, measures the migration velocity of particles in an electric field. The resulting d_{mob} is the product of the shape factor χ and the spherical-equivalent diameter of the particle, after correcting for the non-continuum nature of the gas phase (Equation S1). The shape factor χ describes the ratio of the drag force on the particle to the drag force on an equivalent-volume sphere, and can be calculated from measurements of particle mass and mobility if the particle's material density is known (the calculation is detailed in Section S1). The shape factor $\chi = 1$ for spheres (e.g. liquid particles). For a $d_{\text{mob}} = 300$ nm soot particle, χ can be as large as 2 or 3 (Sorensen, 2011, and our Figure 4). Following extensive compaction, χ is about 1.5 for moderately large soot particles (Ghazi and Olfert, 2013, our Figure 4; and Corbin and Sipkens, in prep.), although this limit is smaller for aggregates containing smaller numbers of spherules.

3.2 Evidence for capillary compaction

3.2.1 Context: use of the mobility diameter d_{mob} to infer compaction

A large number of studies have reported a decrease in the mobility diameter d_{mob} of soot aggregates after the condensation, and sometimes both condensation and evaporation, of liquid coatings (e.g. Kütz and Schmidt-Ott, 1992; Weingartner *et al.*, 1995, 1997; Gysel, 2003; Zhang *et al.*, 2008; Khalizov *et al.*, 2009; Xue *et al.*, 2009; Pagels *et al.*, 2009; Miljevic *et al.*, 2010; Tritscher *et al.*, 2011; Bambha *et al.*, 2013; Ghazi and Olfert, 2013; Peng *et al.*, 2016; Leung *et al.*, 2017b; Pei *et al.*, 2018; Chen *et al.*, 2016, 2018; Enekwizu *et al.*, 2021). Many of these studies interpret changes in the mobility diameter d_{mob} as clear evidence of compaction. Only a few of these studies, discussed here, provide clear evidence for capillary compaction, as distinct from evaporation.

Because d_{mob} is not a direct measurement of compaction, its use to infer compaction may hypothetically lead to biases. For example, it may be hypothesized that d_{mob} may change upon condensation due to a change in χ rather than a change in size. However, Leung *et al.* (2017b) showed unequivocally that a decrease in d_{mob} is due to condensation-compaction and is not a measurement artifact. Leung *et al.* (2017b) formed *p*-xylene SOA at extremely low relative humidity (RH < 12%), where it is known to form a glassy solid as well as high RH (20% to 85%) where it is expected to be liquid (Song *et al.*, 2016).

Leung *et al.* (2017b) then showed that d_{mob} decreased with the addition of small amounts of liquid SOA, but increased with the addition of small amounts of solid SOA. Therefore, the liquid condensation must have caused compaction. This result is consistent with the anthracene results discussed in Section 4, however, we note that solid SOA is glassy (Järvinen *et al.*, 2016) while solid anthracene is crystalline, which may lead to differences in the final shape of the coated particles.

3.2.2 Capillary compaction below saturation

Miljevic *et al.* (2010) observed that freshly-produced soot particles compacted when bubbled through a variety of organic liquids, but not when bubbled through water. These results are particularly important because of two details of the bubbling technique, which stand in contrast to the more-common alternative of exposing the soot particles to supersaturated vapours.

First, bubbling was done at room temperature, which means that the temperature-dependent rate of capillary formation (Section 2) was not enhanced relative to atmospheric conditions. Soot particles spent a relatively short time (about 1 second) in the bubbler, although subsequent changes during the additional seconds of transport to the measurement system may have occurred (Enekwizu *et al.*, 2021).

Second, the vapour pressure within a bubble is slightly below saturation, due to the inverse Kelvin effect (relatively small at large diameter of most bubbles). Since compaction occurred below saturation, and since capillary menisci condense well below saturation, this corroborates the capillary-condensation mechanism described above and suggests a role of contact angle (which governs capillary formation).

We also note that, when Miljevic *et al.* (2010) switched from bubbling candle soot through hexane to bubbling through water, the soot did not undergo compaction. This observation is consistent with the Ma *et al.* (2013a) study discussed below, and

J.C. Corbin: Soot compacted by condensation or evaporation

illustrates the key role of contact angle. The high water-soot contact angle would have prevented capillary condensation from occurring.

Further evidence for capillary compaction is provided by the studies of Chen *et al.* (Chen *et al.*, 2016, 2018) and Enekwizu *et al.* (2021). Chen *et al.* showed that a sub-monolayer volume of PAHs coated onto soot could cause substantial compaction, while Enekwizu *et al.* (2021) detected compaction near room temperature, at saturation ratios $S < 1$ of triethylene glycol (a polar organic compound). At these sub-monolayer and sub-saturation conditions, only capillary condensation could have occurred. Therefore, these experiments provide clear evidence for capillary condensation, as also concluded by those authors.

3.2.3 Capillary compaction above saturation

Chen *et al.* (2018) presented a study of several different coating materials which we interpret here as illustrating the difference between capillary-compaction by menisci (first two mechanisms in Section 2.2) and by capillary bridges (third mechanism in Section 2.2). In Chen *et al.* (2018), a first group of compounds (Group A) caused sudden compaction with minute coating volumes (d_{mob} decreased to 80% of its initial value for coatings $\sim 5\%$ of initial particle volume), while a second group (Group B) required much larger coating volumes to be compacted (d_{mob} decreased to a similar endpoint for coatings 10–48% of initial volume). These trends cannot be explained by differences in surface tension (as noted by Chen *et al.* (2018)) nor by contact angle alone, since the two groups contained compounds with a range of polarities.

The one consistent difference between Groups A and B in Chen *et al.* (2018) is that the Group A compounds had vapour pressures at 25 °C ranging from 0.18 to 2.00 Pa, whereas Group B compounds had vapour pressures ranging from 10^{-7} to 10^{-4} Pa. Consequently, Chen *et al.* (2018) exposed soot particles to Group B compounds at much higher experimental temperatures (≥ 50 °C) compared with Group A. This difference in temperature altered the coating volume, as pointed out by Chen *et al.* (2018). Crucially, it also created much higher transient saturation ratios. According to the calculations of Chen *et al.* (2018), the Group-B temperatures resulted in maximum saturation ratios of $S_{\text{max}} > 20$. At these extreme saturation ratios, multiple nanodroplets may have activated and grown too quickly for capillary menisci to nucleate, leading to bridge-capillary compaction. (As with all studies that both add and remove *liquid* coatings, it is also possible that further compaction occurred during coating removal, via the DEC mechanism. Our experimental results, presented Section 4, removed solid coatings and isolated the capillary and DEC mechanisms.)

If Groups A and B of Chen *et al.* (2018) represent different condensation-compaction mechanisms due to different experimental conditions, then some experimental results must be interpreted with caution. Specifically, changes in soot structure with coating volume should not be parameterized and extrapolated from laboratory studies using high- S_{max} systems (i.e. systems with heated sample reservoirs). On the other hand, the final change in mobility diameter (maximum compactness) achieved between studies is consistent, as expected (Zangmeister *et al.*, 2014): this was similar at high S_{max} in Groups A and B, and was consistent with the below-saturation studies discussed in the previous subsection.

In their discussion and subsequent work (Ivanova *et al.*, 2020; Enekwizu *et al.*, 2021), Chen *et al.* (2018) focussed on the competition between the Kelvin effect and vapor supersaturation. As their data set also varied S_{max} substantially, it is not clear whether this competition played a key role relative to phase-formation barriers. Additional data to constrain this hypothesis would be valuable.

3.3 Evidence for evaporation-compaction and nanodroplet activation (NDA)

Three studies have indicated evidence for evaporation compaction. Two of these data sets demonstrate only subtle evidence, while the third presents direct evidence. The subtler evidence from Leung *et al.* (2017b) and Chen *et al.* (2016), using glassy SOA and anthracene respectively, showed that d_{mob} increased for thin coatings but decreased when these coatings were denuded, presumably after due to melting in the denuder. The glassy SOA case was discussed above; the anthracene result is returned to below in Section 4.3 and Figure 5.

The third study provides the most direct evidence, by observing the morphology of water-coated soot after injecting it into bulk water and measuring the particle fractal dimension by static light scattering (Ma *et al.*, 2013a). Ma *et al.* (2013a) found that this fractal dimension remained low within the water droplets (less than 1.94), corresponding to an open morphology. They also demonstrated that the same soot particles underwent compaction during water evaporation using transmission electron microscopy (TEM) and by measuring a mass-mobility exponent of 2.79 (see Sorensen 2011 and Olfert and Rogak 2019 for a detailed discussion of the mass-mobility exponent).

The soot particles studied by Ma *et al.* (2013a) did not take up water below $S = 1.2$. This shows that they were hydrophobic. Hydrophobicity implies a high contact angle ($\theta > 90^\circ$) as expected (Persiantseva *et al.*, 2004). Therefore, film formation would be unlikely and capillary condensation would not have occurred. Rather, water will have condensed via NDA (Figure 1), as described in Section 2.

There are two reasons why the results of Ma *et al.* (2013a) should not be extrapolated to atmospheric science. First, such high S do not normally occur in the atmosphere, where most particles activate at $S < 1.01$ (Schmale *et al.*, 2018). Second, atmospheric soot typically becomes rapidly oxidized or coated with small amounts of hydrophilic material (e.g. Vakkari *et al.*, 2014) which are observed to result in water condensation at much lower S than for hydrophobic soot (Mikhailov *et al.*, 2006; Xue *et al.*, 2009). Surface oxidation may also occur (Matuschek *et al.*, 2007; Corbin *et al.*, 2015) to lower S_{crit} without involving coatings. Atmospherically realistic condensates like secondary organic aerosol have been shown to condense readily onto soot, without requiring extreme supersaturations (Qiu *et al.*, 2012; Schnitzler *et al.*, 2014; Guo *et al.*, 2016; Leung *et al.*, 2017b), due to low contact angles and the presence of organics with a broad range of volatilities (Tröstl *et al.*, 2016). Thus, the work of Ma *et al.* (2013a) represents a specialized system in which the phenomenon of evaporation-compaction could be demonstrated.

We note that Ma *et al.* (2013a) attempted to explore the role of θ on their results by oxidizing their soot samples in a furnace. They flowed soot particles through a furnace at 300, 600, and 700 °C. However, as shown in a later study using the same system (Ma *et al.*, 2013b), at these temperatures soot oxidation results in a decrease of particle mass due to volume oxidation by O₂, in contrast to the surface oxidation that occurs at higher temperatures (Kelesidis and Pratsinis, 2019). This decrease of particle mass is evident in the oxidation results of Ma *et al.* (2013a) and makes the quantitative interpretation of their data difficult. Nevertheless, it is clear that this furnace treatment did not have the expected result of rendering the soot particles hydrophilic, since the maximum saturation ratio required to activate particles after furnace oxidation was even higher after the furnace ($S > 1.5$) compared to before ($S > 1.2$). This may be due to the loss of polar functional groups at the soot surface (Matuschek *et al.*, 2007), which would be active sites for NDA.

3.4 Related aggregate restructuring topics

The preceding discussion focussed on studies providing clear evidence for the restructuring mechanisms relevant to soot coating in the atmosphere. For completeness, the present subsection discusses other noteworthy studies on related topics.

3.4.1 Role of surface tension and viscosity

Schnitzler *et al.* (2017) reported a correlation between the surface tension of a variety of organic coatings (including glycerol, ethylene glycol, furfural, oleic acid, and *o*-xylene) and the amount of compaction these coatings caused on soot particles. This observation stands in contrast to that of Chen *et al.* (2018), who observed large differences in compaction for different restructuring mechanisms (discussed in detail above) and no correlation with coating surface surface tension. From these two studies, we conclude that the extent of restructuring depends first on the restructuring mechanism, and second on coating properties such as surface tension.

From the perspective of coating viscosity, the data of Leung *et al.* (2017b) provide valuable insights. Leung *et al.* (2017b) observed soot compaction by SOA at relative humidities between 20% and 80%. The viscosity of SOA at 20% RH is approximately 5 orders of magnitude lower than at 80% humidity (Song *et al.*, 2016), so the Leung *et al.* (2017b) data indicate that

J.C. Corbin: Soot compacted by condensation or evaporation

restructuring is possible across a broad range of viscosities. Their data do suggest small differences in compaction for SOA coatings formed between 20–40% RH and 60–85 % RH. These differences were similar in magnitude ($\sim 10\%$ change in d_{mob}) as those observed by Schnitzler *et al.* (2017) where coating surface tension was varied, indicating a minor effect in the context of this review.

3.4.2 Evidence from effective-density measurements of soot

The effective density of soot is widely used to estimate the mass of particles for which d_{mob} is known. Olfert and Rogak (2019) reviewed a large number of studies and showed that the effective-density trends in *uncompacted* soot with d_{mob} are similar for many engines and laboratory flames. We note that Olfert and Rogak (2019) observed a slightly higher effective density for compression-ignition engines than for other sources, suggesting that those soot particles may have undergone partial compaction due to condensation in the exhaust of those engines. This may suggest that some degree of compaction occurred in those engines, since condensation is most rapid for smaller particles and since those engines emit a larger fraction of volatile material. Care should therefore be taken when applying the effective-density fit of Olfert and Rogak (2019) to soot samples where compaction may have occurred. A detailed discussion of the effective density of compacted soot is presented in Corbin and Sipkens (manuscript in preparation).

3.4.3 Laser-induced de-compaction

Bambha *et al.* (2013) reported that soot restructuring could be reversed by laser-heating. They coated soot by condensation, then used a pulsed 1064 nm laser to heat the soot and cause coating evaporation. Since condensation-compaction is to be expected for this soot–oleic-acid system, this implies that the soot particles underwent *decompaction* due to the laser heating process, perhaps due to the nucleation of bubbles at the soot surface (in analogy to the heterogeneous nucleation of bubbles at liquid-solid interfaces during boiling). Such bubbles would remain attached to the soot surface in order to minimize their Gibbs energy, and may lead to decompaction of the soot structure during their growth.

Bambha *et al.* (2013) also stated that they observed compacted soot in the electron microscope after coating, but they were unable to image the particles before coatings evaporated. Such images would constitute evidence for condensation-compaction, if they could be produced without any interference of the evaporating droplet.

3.4.4 Metal nanoparticles and sintering

Aggregates of metal nanoparticles are known to sinter (partially coalesce without liquefying) at temperatures well below the melting point, and this leads to aggregate compaction (Kleinwechter *et al.*, 1997; Schmidt-Ott, 1988; Friedlander, 2000). The same is true for metal-oxide nanoparticles (Kelesidis *et al.*, 2018). This process is attributable to melting-point depression (Section S4) and not capillary forces. Conversely, the strong inter-particle bonds of strongly sintered aggregates (Friedlander, 2000) can prevent condensation-compaction (Kelesidis *et al.*, 2018). The fact that compaction has been observed for the wide variety of soot sources cited herein, without exception, indicates that such inter-particle bonds are weaker than typical capillary forces for soot.

3.4.5 Carbon nanoparticles other than soot

Weingartner *et al.* (1997) and Mikhailov *et al.* (1997) observed the compaction of spark-generated carbon nanoparticles at $S < 1$ due to water and benzene vapour exposure, respectively. These spark-generated nanoparticles have significantly different properties to soot due to their unique and rapid formation pathway (Gysel *et al.*, 2012, and citations therein). Their contact angles with different liquids and inter-particle bonds are different to soot, so they are not discussed in the soot section above.

3.4.6 Can soot compaction be avoided during condensation?

A small number of laboratory studies have implied that soot compaction during condensation can be avoided in some cases. These studies are reviewed in the following discussion, and are attributed to either soot-substrate adhesion forces or to statistical anomalies. Caution should therefore be exercised when interpreting these studies as generally representative.

A salient example of avoided compaction is provided by Cross *et al.* (2010). This study presented a single electron micrograph of a laboratory soot particle that was not compacted despite being sampled during a coating-denuding experiment using dioctyl sebacate. The authors suggested that this processing had failed to compact the soot. However, studies using the in-situ d_{mob} technique, which measured orders-of-magnitude more particles, have consistently reported compaction of soot by the exact same compound (Ghazi and Olfert, 2013; Chen *et al.*, 2018). The most likely explanation is that the single particle measured by Cross *et al.* (2010) was not representative of the overall particle ensemble. This example is particularly important because it was possible to reproduce the experiment and revise the initial conclusions, unlike most atmospheric studies.

Another category of exceptions is studies where soot particles were sampled onto microscopy grids before coatings were condensed. These studies have included electron (Huang *et al.*, 1994; Ebert *et al.*, 2002; Zuberi *et al.*, 2005), X-ray (Zelenay *et al.*, 2011), and atomic force (Köllensperger *et al.*, 1999) microscopy. Of those studies, only Köllensperger *et al.* (1999) claimed to observe restructuring on the microscopy grid. In these on-grid condensation experiments, soot-substrate adhesion forces, which are substantial (Friedlander *et al.*, 1998; Rocca *et al.*, 2013) may exceed compaction forces, preventing both condensation-compaction and evaporation-compaction. In contrast, studies where soot is restructured in the aerosol phase before being sampled for microscopy analysis can provide valuable insights into morphology, both in the laboratory (studies cited above) and in the atmosphere (Section 5).

3.4.7 Does soot compaction occur during uptake into bulk liquids, or during coagulation?

A few studies have provided evidence that compaction can be partly or fully avoided during soot uptake into bulk liquids. Ma *et al.* (2013a), discussed in detail above, measured a low fractal dimension for soot that was incorporated into bulk water after activation as soot-in-water droplets. Using electron microscopy, Rocca *et al.* (2013) observed that soot particles in the lubricating oil of a diesel engine were only partly compacted. Finally, Brauer *et al.* (2001) observed non-compacted soot in the lungs of lifelong Mexico City residents. The observations of Brauer *et al.* (2001) are significant and suggest that soot particles entered the lungs as freshly emitted, hydrophobic soot, did not nucleate water during inhalation, and deposited onto the respiratory system. These uncompacted particles may have been more toxic due to their higher active surface area, and potentially different interactions with human macrophages.

These observations of avoided compaction during uptake into bulk liquids indicate that the direct contact of aggregates with air-liquid interfaces is not sufficient to cause compaction. Therefore, the process of coagulation between soot aggregates and liquid droplets is also unlikely to cause compaction. Conversely, partial evaporation-compaction may occur in the scenario that the liquid droplet partially wets an aggregate and is then evaporated. This scenario may occur during cloud processing or laboratory experiments.

3.4.8 Uncompacted soot in the atmosphere

The evidence reviewed above suggests that soot particles coated primarily by condensation (gas-to-particle addition of liquid coatings) will undergo substantial compaction. However, soot particles may become internally mixed by other mechanisms, such as deposition (gas-to-particle addition of solid or extremely viscous glassy coatings), or coagulation (diffusive collision of soot particles with other particles and subsequent adhesion). The question of what fraction of soot particles in the atmosphere remains uncompacted upon mixing has substantial implications for the light-absorption properties of soot, and is discussed in detail later in this manuscript (Section 5).

3.5 Summary of soot compaction review

Our review of the soot compaction literature has illustrated that:

- capillary condensation generally leads to soot compaction,
- capillary compaction is slightly less efficient in experiments where very high saturation ratios ($S > 1.2$) do not allow enough time for capillary formation,
- capillary compaction can be avoided when high-contact-angle vapours, such as water, condense by nanodroplet activation (NDA) instead of capillary activation,
- capillary compaction can be avoided or reduced for extremely viscous (glassy) glassy or solid coatings of atmospheric relevance,
- capillary compaction can be avoided or reduced when soot mixes by coagulation with other particles, or impaction with a bulk liquid,
- evaporation compaction will act on soot particles within evaporating droplets, when those droplets shrink below the size of the soot aggregate, and is important only when capillary compaction is avoided during the preceding incorporation of the aggregate into the droplet,
- for atmospherically relevant systems, changes in coating mechanisms play a larger role than changes in coating surface tension or viscosity,
- unique compaction trends and mechanisms have been observed for non-soot materials (spark-generated aggregates, sintered-metal aggregates, etc.) and during special processes such as heating by pulsed lasers.

4 Experimental Study

In this Section we present the results of a series of experiments designed to separately study condensation and evaporative compaction. In these experiments, we controlled the phase of an organic coating during its addition or removal, so that capillary forces could be switched on or off. We performed most experiments using anthracene, and some with oleic acid. The results demonstrate that both condensation and evaporation can cause soot restructuring, and represent the first data set in which both of these mechanisms have been demonstrated for the same soot source and coating material.

4.1 Experimental design

4.1.1 Compaction pathways

Our experiments are summarized in Table 1, which also introduces the labels used in the subsequent discussion. The five rows of Table 1 represent five pathways by which coatings can be added and removed. Each pathway is defined by the addition—removal of two phases as nanodroplets **N**, capillary liquids **L**, or solids **S**. For example, liquid-addition—solid-removal (i.e., condensation—sublimation) is referred to as pathway **LS**. During addition or removal, the CC or DEC restructuring mechanisms may occur, or may be avoided by NDA (Section 2), as illustrated in more detail in Figure 2.

We designed experiments to follow these pathways using anthracene based on its phase diagram (Figure S1) as further discussed in the SI. Due to the experimental difficulty of removing liquid anthracene coatings, we performed some additional experiments using oleic acid. The experiments were interpreted as follows. For Pathway **LS**, we performed experiments where coatings were added as liquids (*condensed*), then frozen prior to their removal as solids (*sublimation*). Since capillary forces

cannot act during sublimation, we attribute any restructuring via Path **LS** to the condensation process. Path **SL** is the inverse of Path **LS**: coatings are added in the solid phase (*deposition*) then melted prior to their removal as liquids (*evaporation*), so, capillary forces can act only during coating removal. Path **SS** is a control experiment where no capillary forces are allowed to act: coatings are deposited and subsequently sublimated. Since capillary forces are not allowed to act, no restructuring should occur. Path **LL** both adds and removes coatings in the liquid phase, allowing capillary forces to act during both coating addition and removal. Finally, Path **NL** may allow droplets to form without capillary forces acting. Path **NL** was not reproduced in this study, as we focussed on a single coating material to avoid changing the physical properties of our coatings between experiments.

4.1.2 Experimental methods

Our experimental setup (Figure S2 and S3) was similar to that used in previous studies (e.g. Nguyen *et al.*, 1987; Moteki and Kondo, 2007; Chen *et al.*, 2016). The present subsection therefore summarizes only the key experimental details of our experiments; complete details are given in the supplementary information (Section S3).

Soot was generated by a miniCAST 5201c soot generator (Jing Ltd., Switzerland) which consists of a partially-quenched propane diffusion flame. We pre-selected aggregates of mature soot with mobility diameter of 300 nm before using coating apparatuses constructed in-house to add anthracene or oleic acid coatings to the soot.

The coating apparatuses (Figure S3) generally consisted of a heated section (using either a hot plate, oil immersion, or heating tape) followed by a cooling section (using either heat conduction to room air, additional insulation to slow cooling, or ice packs to accelerate cooling). Oleic acid coatings were added with the apparatus heater set between 94 and 140 °C. Anthracene coatings were added with the apparatus heater set between 95 and 202 °C. Above 202 °C, the reservoir emptied too quickly for measurements to be practical. In some experiments, we pre-coated the walls of the second apparatus with anthracene in order to increase its vapour phase concentrations, which allowed us to avoid anthracene sublimation upon heating and to melt anthracene prior to its evaporation.

The mass of added coatings was then measured using an Aerosol Particle Mass analyzer (APM, Model 3601, Kanomax Japan; Ehara *et al.* 1996) as described further in the SI. The particle-mass measurements were converted to coated-particle volume V_1 according to

$$V_1 = (V_0 + V_{OM}) = \frac{m_0}{\rho_{BC}} + \frac{(m_1 - m_0)}{\rho_{OM}} \quad (1)$$

where V_0 and m_0 are the volume and mass of an uncoated soot particle, V_{OM} is the volume of coating, $m_1 = (m_0 + m_{OM})$ is the total mass of a coated soot particle, $\rho_{soot} = 1800 \text{ kg m}^{-3}$ is the material density of soot (Ouf *et al.*, 2019) and ρ_{OM} is the material density of the organic coating. For unprocessed or denuded soot, $m_{OM} = 0$, so $V_1 = V_0$. For coated soot, V_1/V_0 is the volume increase due to the coating.

Shape factors were calculated by iteratively solving Equation S1 with $d_{mob} = 300 \text{ nm}$.

The primary denuder used in this work was a catalytic stripper (CS015, Catalytic Instruments GmbH, Rosenheim, Germany), which vapourizes and then oxidizes organic molecules at 350 °C. In some experiments, this stripper was replaced with the activated-charcoal thermodenuder described by Burtscher *et al.* (2001) or a second coating apparatus.

4.2 Results: observation of condensation and evaporative compaction

4.2.1 Changes in mobility diameter

Figure 3 shows d_{mob} distributions measured during the experiments. The experiments used anthracene or oleic acid to investigate the compaction mechanisms from Section 2. Oleic acid was used for Path **LL**; anthracene was used for all others. The inset TEM images in Figure 3 depict aggregates sampled from each condition. Not all particles observed in the TEM were fully compacted

after processing (Figure S4); this may be due to variability between compaction events, soot-particle properties, or heterogeneity in the conditions of our processing apparatus. We rely on the much better sampling statistics of the mobility-size-distributions for all of our conclusions below.

Figure 3a shows results for the addition and removal of solid coatings via Path **SS** of Table 1 and Figure 2. The results show that Path **SS**, coating deposition–sublimation, resulted in no change to d_{mob} . The lack of compaction for Path **SS** shows that capillary forces are necessary for compaction in general, and rules out the hypothesis that van der Waal's forces alone are sufficient. In Figure 3a, we intentionally presented conditions where a very large volume of solid coatings was added (10-fold the initial soot-particle volume) to ensure that the lack of observed compaction was not due to a lack of sufficient coating material.

In Figure 3b, capillary forces were allowed to act since coatings were melted prior to their evaporation (Path **SL**). This resulted in a reduced final d_{mob} and compacted particles, as confirmed by TEM. Combined with the results of Figure 3a (Path **SS**), this confirms that evaporation-compaction exclusively occurred in this experiment. The coating volume in Figure 3b was 10-fold the initial soot-particle volume.

In Figure 3c, the reverse of Figure 3b was measured. Liquid coatings were added by condensation, but frozen prior to their removal by sublimation (Path **LS**). This resulted in a reduced modal d_{mob} and compacted particles, as confirmed by TEM. This confirms that condensation compaction occurred in Path **LS**.

Thus, the experiments shown in Figure 3a–c demonstrate that both condensation-compaction and evaporation-compaction may occur: aggregate compaction may be triggered by liquid condensation or liquid evaporation, but not solid deposition nor solid sublimation. This conclusion is corroborated by previous studies using anthracene in Section 4.3.

Finally, Figure 3d shows results for Path **LL** (coating condensation and evaporation). Compacted particles were observed after this experiment. Because the final modal d_{mob} in Paths **LS** and **LL** are similar (purple lines in Figure 3c and 3d), most of the compaction in Path **LL** likely occurred during condensation, which occurred before evaporation. We used a smaller coating volume in Figure 3c and 3d (2-fold the initial soot-particle volume) because this was sufficient to cause compaction.

4.2.2 Coating volume effects

Figure 4a shows the results of Figure 3 in terms of the change in modal d_{mob} as a function of coating volume. That is, Figure 4a extends Figure 3 to a much larger number of comparable experiments in which the coating mass was varied. Data are shown for both anthracene and oleic acid coatings. Each group of data is labelled with two letters following Table 1: the first letter (S or L) indicates the coating phase during addition, the second letter (S or L) indicates the coating phase during removal. Curves are included to guide the eye. Error bars are included for sparse data and are omitted where multiple similar measurements provide an indication of measurement precision.

In Figure 4, the mode d_{mob} was retrieved from fits to the data. When more than one mode was apparent due to heterogeneity in coating thicknesses (e.g. Figure 3a and 3b), the mode containing more particles was reported, for consistency with the denuded size distributions. Figure 4b plots the same data after conversion to shape factor χ .

Figure 4a shows that oleic acid condensation led to a decrease of d_{mob} until the particle volume approximately doubled ($V_1/V_0 > 2$), that is, until the particle contained equal volumes of coating and soot. For thin coatings, d_{mob} was similar for coated and denuded particles. For these particles, the shape factor χ (Figure 4b) was larger for denuded than for coated particles. In the context of Sections 2 and 3, this is interpreted as condensation compaction.

Figure 4b shows that χ decreased monotonically with increasing V_1/V_0 for both coating materials. This χ reached an asymptotic value of unity for oleic acid coatings, demonstrating particle sphericity. Sphericity is expected when the particle surface is liquid, and when aggregates are fully encapsulated. Importantly, $\chi = 1$ was also reached for liquid-anthracene coatings. This was not observed for solid anthracene coatings, where $\chi = 1.2$ was the asymptotic value. Slowik *et al.* (2007) achieved a similar asymptotic value ($\chi = 1.3$) for solid anthracene (Figure S5). Therefore, our measured shape factors support our assertion

that we were able to deposit solid or liquid anthracene coatings by varying our experimental conditions. For all V_1/V_0 , χ is higher for denuded than for coated particles because a compact soot aggregate is not a smooth sphere (Figure S4).

Because our coating apparatus did not allow us to finely control the amount of anthracene addition in experiments involving solid deposition, only a single data point is available for those cases. However, our conclusions from this limited data set are corroborated by the literature comparison below.

A unique implication of our data set relative to previous literature is that we observed smaller amounts of restructuring after condensation-compaction than after evaporation-compaction. This suggests that evaporation-compaction is even more efficient at restructuring than the capillary-compaction mechanisms. However, because we were only able to follow Path **LL** using oleic acid, and not anthracene, this difference may also reflect differences in surface tension (Schnitzler *et al.*, 2017), contact angle, or morphology for the solid-coated particles.

4.2.3 Further validation experiments

To confirm that bulk anthracene sublimated upon heating in our apparatus, we performed an experiment where anthracene powder (as received) was heated in the coating-apparatus reservoir while the apparatus was kept open (in a fume hood) for observation. The crystals were heated continuously in air at roughly $1\text{ }^\circ\text{C s}^{-1}$. We observed no visual changes until the apparatus reached $191\text{ }^\circ\text{C}$, at which point the crystals began to shrink rapidly. As the temperature was increased to $220\text{ }^\circ\text{C}$, fumes were observed without any indication of melting. A spatula placed within the fumes became coated with a matte film initially and millimetre-sized planar crystals later (Figure S6). The initial matte film on the spatula may be related to the melting point reduction of nanoscopic quantities of anthracene (Figure S7). Although our visual observation could not confirm this hypothesis, Lopatkin *et al.* (1977) have directly observed that thin films of anthracene condense as liquids at temperatures above $55\text{ }^\circ\text{C}$ and solids below this temperature. Lopatkin *et al.* (1977) studied films of thickness 10 nm to $16\text{ }\mu\text{m}$ with growth rates of 3 to 15 nm/s . Their conclusions are consistent with our melting-point depression calculations, discussed above and in the SI.

To ensure that the phase of condensing anthracene was not affected by residual OM from the flame, we pre-denuded the soot at $350\text{ }^\circ\text{C}$ before repeating the condensation ($V_1/V_0 \sim 3.3$) and condensation–denuding (at $200\text{ }^\circ\text{C}$ and $150\text{ }^\circ\text{C}$) experiments. No change was observed in our results and the soot particles returned to their original mass (the mean \pm standard deviation of measurements before and after denuding was $6.40 \pm 0.15\text{ fg}$ and $6.38 \pm 0.18\text{ fg}$, respectively).

We also ensured that anthracene oxidation was not relevant in our apparatus by repeating the experiment in nitrogen rather than synthetic air. The results were included in Figure 4 at $V_1/V_0 = 2.55$ and are fully consistent with the other results.

4.3 Discussion: comparison with previous soot–anthracene studies

Two previous studies have reported data similar to Figure 4 for anthracene (Slowik *et al.*, 2007; Chen *et al.*, 2016). These data have been included in Figure 5. The purple diamonds in Figure 5 show the data of Slowik *et al.* (2007), who coated soot with anthracene at $52\text{--}85\text{ }^\circ\text{C}$. As shown in Figure S7, this temperature is well below the melting point of even 3 nm anthracene spheres, so Slowik *et al.* (2007) most likely deposited solid coatings. Slowik *et al.* (2007) removed these coatings at $200\text{ }^\circ\text{C}$, which is below the $216\text{ }^\circ\text{C}$ melting point of anthracene. Therefore, as also concluded by those authors, the anthracene coatings of Slowik *et al.* (2007) did not result in restructuring of soot; they followed Path **SS** of Figure 2.

Chen *et al.* (2016) coated soot with small amounts of anthracene (and 5 other PAHs) at $25\text{--}85\text{ }^\circ\text{C}$. They removed coatings in a denuder set to $300\text{ }^\circ\text{C}$. In their experiments, anthracene addition increased d_{mob} , while anthracene removal decreased d_{mob} below its initial value. The increase of d_{mob} with coating indicates that Chen *et al.* (2016) added solid anthracene, resulting in no restructuring since no capillary forces could act. The decrease of d_{mob} below its initial value indicates that Chen *et al.* (2016) melted the anthracene coatings prior to their removal. Chen *et al.* (2016) therefore followed Path **SL** illustrated in Figure 3d.

We have not compared our results with Slowik *et al.* (2007) or Chen *et al.* (2016) in terms of shape factor χ , because those two studies and our study used soot with different spherule diameters and aggregate mobility diameters. So, the initial and final

χ expected in the three studies is different, as shown systematically by Leung *et al.* (2017a). Regardless, we have reanalyzed the data of Slowik *et al.* (2007) in Figure S5 to show that they do illustrate the same trends observed here. For the data of Chen *et al.* (2016), shape factor changes are small since those authors focussed on thin coatings (i.e., small volume growth factors in Figure 5).

Here it is worth repeating the statement by Chen *et al.* (2016) that complex mixtures are likely to have lower melting points (Peters *et al.*, 1997; Marcolli *et al.*, 2004). Nanoscopic quantities of material are also more likely to exist in the liquid phase (Section S4). Consequently, in combustion and atmospheric chemistry, coatings are most likely to condense as liquids. Important exceptions may include the scenarios where secondary organic aerosols reach very high viscosities due to low temperatures or humidity (Leung *et al.*, 2017b; Koop *et al.*, 2011; Schmedding *et al.*, 2020) and where ice crystals may form without transitioning through cloud droplets on soot (Marcolli, 2014; David *et al.*, 2019).

5 Discussion: atmospheric implications

If liquid condensation generally leads to the compaction of soot particles, as concluded by the reviews and experiments summarized above, then it may be expected that atmospheric soot particles coated by condensation are compact. In this context, the condensate may be secondary particulate matter (e.g. Adachi *et al.*, 2010), cloud water (Bhandari *et al.*, 2019; China *et al.*, 2015a), or semivolatiles co-emitted with the soot which condense as combustion emissions cool (Weingartner *et al.*, 1997; China *et al.*, 2014). If atmospheric soot particles are observed not to be compact, they may have become internally mixed by the deposition of highly viscous (nonliquid or glassy) organic materials (Shrivastava *et al.*, 2017) or by coagulation.

Coagulation is recognized as an important mixing mechanism for soot during photochemically inactive periods (e.g. at night) (Riemer *et al.*, 2004; Fierce *et al.*, 2015) as well as in heavily polluted regions such as Eastern China, India, and Central Africa (He *et al.*, 2016). Microscopy images provide unambiguous evidence for coagulation when soot is mixed with non-volatile material such as dust (Xiong and Friedlander, 2001). Other images strongly suggest coagulation, when soot particles appear to be attached to droplets of other material (e.g. Adachi *et al.*, 2010; Adachi and Buseck, 2013; China *et al.*, 2013, 2014; Moteki *et al.*, 2014), although coagulation can also result in other morphologies. In practice, both coagulation and condensation are likely to contribute to the internal mixing of atmospheric soot particles with coating materials. For example, a soot particle may coagulate with a much smaller particle and remain uncompacted but later undergo condensation-compaction due to the formation of secondary aerosol, the hygroscopic uptake of water by the coagulated material, or by activation into a cloud droplet.

It has been inferred from recent experimental work that approximately half of the measured soot particles were non-spherical (i.e., non-compacted) in the atmosphere over Beijing, based on tandem measurements of single-particle soot-particle mass and optical size after d_{mob} classification (Hu *et al.*, 2021). These measurements were shown to predict the light absorption enhancement due to coatings (E_{abs}) in a simple empirical model which considered non-spherical particles as uncoated and spherical particles as core-shell coated soot particles (Hu *et al.*, 2022). At the same time, negligible E_{abs} has been observed in other studies despite substantial coating volume fractions (Cappa *et al.*, 2012, 2019). Fierce *et al.* (2020) proposed that this discrepancy was related to deviations from a core-shell configuration of coated soot, and showed that a laboratory-based model of these deviations better described the atmospheric data of Cappa *et al.* (2019). In particular, the Fierce *et al.* (2020) model explained half of the E_{abs} discrepancy by accounting for heterogeneity in soot coating distribution between particles, and another quarter of the discrepancy by accounting for deviations from core-shell morphology.

Fierce *et al.* (2020) estimated deviations from core-shell morphology based on laboratory experiments where soot was coated extremely quickly, either in coating apparatuses like ours (Figure S3a) or in a potential aerosol mass (PAM) oxidation flow reactor (Forestieri *et al.*, 2018). These apparatuses have residence times of less than 2 minutes, while atmospheric coatings take 2 hours to form even under the most favourable conditions (Vakkari *et al.*, 2014). Therefore, atmospheric particles may deviate even further from core-shell mixtures than represented by the Fierce *et al.* (2020) model. Extending the approach of Fierce *et al.*

(2020) to model atmospheric coagulation more directly may therefore be valuable in improving our predictions of the global climate effects of soot restructuring.

Since solid coatings do not cause restructuring, future work should also explore the potential of solid coating formation in the context of biomass-burning particles and secondary organic aerosols. In this context, care should be taken when interpreting indirect evidence of coating phase. For example, particle phase may be inferred from measurements of particle bounce (solids bounce, while liquids wet the surface) or chemical reactivity (solids react more slowly than liquids). For *m*-xylene SOA, bounce measurements have indicated a glass-to-liquid phase transition at 60–80% RH while reactivity measurements indicated a transition at 35–45% RH (Li *et al.*, 2015). Since compaction is a physical process, the higher RH would be expected to be more relevant to soot restructuring. However, as discussed in Section 3, Leung *et al.* (2017b) observed a transition in soot restructuring by *p*-xylene-SOA at 20% RH, consistent with the poke-and-flow experiments of Song *et al.* (2016). The difference may be due to the melting-point depression of small amounts of SOA condensates, a difference in the composition of smaller (capillary) quantities of SOA, or some other mechanism.

Finally, we have not discussed the NDA mechanism in an atmospheric context because the necessary conditions of high supersaturation and high contact angle are unlikely to occur. For the typical case of organic condensates on soot, atmospheric SOA may also reach high supersaturations ($S > 4$ for the lowest-volatility compounds, Donahue *et al.* 2011), but chamber data have already provided clear evidence that liquid coatings condensed under environmental conditions result in soot compaction (Qiu *et al.*, 2012; Schnitzler *et al.*, 2014; Guo *et al.*, 2016; Leung *et al.*, 2017b). For the extreme case of cloud formation onto un-aged soot particles (e.g. during contrail formation), laboratory experiments at 108% RH have shown that compaction still occurs (China *et al.*, 2015a).

6 Summary

An understanding of soot compaction based on well-established, directly observed phenomena in surface science (Section 2) indicates that there are two mechanisms for condensation compaction (capillary and capillary-bridge) which may regularly occur in the environment under subsaturated conditions. A third mechanism, nanodroplet activation, requires extreme supersaturations and has been demonstrated in the laboratory, but not observed in natural systems. Soot aggregates coated in combustion systems or in the atmosphere are therefore expected to be compacted by the coating process. This compaction may be avoided by coagulation, by the addition of solid coatings, or (in the laboratory) by nanodroplet activation. If compaction is avoided, then coating evaporation also leads to compaction.

This framework of condensation-compaction and evaporation-compaction mechanisms resolves conflicting conclusions in the literature (Section 3) and was demonstrated in the laboratory (Section 4). Future modelling studies focussed on atmospheric and climate science should assume that soot particles become compact when liquid condensation is the primary mechanism of internal mixing. The relative roles of internal mixing by liquid condensation versus coagulation or solid-coating formation should also be explored.

Author contributions. JCC conceived the study, initiated the experiments and critical reviews, and drafted the paper. RLM and MGB discussed initial results, co-designed subsequent experiments, and contributed substantially to data interpretation and to writing.

Acknowledgements. This work was funded by the ERC under grant ERC-CoG-615922-BLACARAT. Thanks are owed to Maarten Heringa for providing a component of the condensation apparatus, to Elisabeth Müller for TEM assistance, and to Louis Tiefenauer for the loan of the TEM sampler. We are grateful to Jay Slowik and Alexei Khalizov for their openness in sharing published data, to Ogochuwku Y. Enekwizu for stimulating discussions, to Timothy Sipkens for contributions to figures, and to the anonymous reviewers for their constructive feedback.

References

- Abel, S.J., Haywood, J.M., Highwood, E.J., Li, J., and Buseck, P.R., 2003. Evolution of biomass burning aerosol properties from an agricultural fire in southern africa, *Geophysical Research Letters*, 30 (15).
- Adachi, K. and Buseck, P.R., 2008. Internally mixed soot, sulfates, and organic matter in aerosol particles from mexico city, *Atmospheric Chemistry and Physics*, 8 (21), 6469–6481.
- Adachi, K. and Buseck, P.R., 2013. Changes of ns-soot mixing states and shapes in an urban area during CalNex, *Journal of Geophysical Research: Atmospheres*, 118 (9), 3723–3730.
- Adachi, K., Chung, S.H., and Buseck, P.R., 2010. Shapes of soot aerosol particles and implications for their effects on climate, *J. Geophys. Res. Atmos.*, 115 (D15), D15206.
- Aubin, D.G. and Abbatt, J.P., 2006. Laboratory measurements of thermodynamics of adsorption of small aromatic gases to n-hexane soot surfaces, *Environ. Sci. Technol.*, 40 (1), 179–187.
- Bambha, R.P., Dansson, M.A., Schrader, P.E., and Michelsen, H.A., 2013. Effects of volatile coatings and coating removal mechanisms on the morphology of graphitic soot, *Carbon*.
- Bhandari, J., China, S., Chandrakar, K.K., Kinney, G., Cantrell, W., Shaw, R.A., Mazzoleni, L.R., Girotto, G., Sharma, N., Gorkowski, K., Gilardoni, S., Decesari, S., Facchini, M.C., Zanca, N., Pavese, G., Esposito, F., Dubey, M.K., Aiken, A.C., Chakrabarty, R.K., Moosmüller, H., Onasch, T.B., Zaveri, R.A., Scarnato, B.V., Fialho, P., and Mazzoleni, C., 2019. Extensive soot compaction by cloud processing from laboratory and field observations, *Scientific Reports*, 9 (1).
- Bocquet, L., Charlaix, E., Ciliberto, S., and Crassous, J., 1998. Moisture-induced ageing in granular media and the kinetics of capillary condensation, *Nature*, 396 (6713), 735–737.
- Bond, T.C., Doherty, S.J., Fahey, D.W., Forster, P.M., Bernsten, T., DeAngelo, B.J., Flanner, M.G., Ghan, S., Kärcher, B., Koch, D., Kinne, S., Kondo, Y., Quinn, P.K., Sarofim, M.C., Schultz, M.G., Schulz, M., Venkataraman, C., Zhang, H., Zhang, S., Bellouin, N., Guttikunda, S.K., Hopke, P.K., Jacobson, M.Z., Kaiser, J.W., Klimont, Z., Lohmann, U., Schwarz, J.P., Shindell, D., Storelvmo, T., Warren, S.G., and Zender, C.S., 2013. Bounding the role of black carbon in the climate system: A scientific assessment, *J. Geophys. Res. Atmos.*, 118, 5380–5552.
- Brauer, M., Avila-Casado, C., Fortoul, T.I., Vedal, S., Stevens, B., and Churg, A., 2001. Air pollution and retained particles in the lung., *Environmental Health Perspectives*, 109 (10), 1039–1043.
- Burtscher, H., Baltensperger, U., Bukowiecki, N., Cohn, P., Hüglin, C., Mohr, M., Matter, U., Nyeki, S., Schmatloch, V., Streit, N., and Weingartner, E., 2001. Separation of volatile and non-volatile aerosol fractions by thermodesorption: instrumental development and applications, *J. Aerosol Sci.*, 32 (4), 427–442.
- Butt, H.J., Graf, K., and Kappl, M., 2003. *Physics and Chemistry of Interfaces*, WILEY-VCH GmbH & Co. KGaA.
- Butt, H.J. and Kappl, M., 2009. Normal capillary forces, *Adv. Colloid Interface Sci.*, 146 (1-2), 48–60.
- Cao, P., Xu, K., Varghese, J.O., and Heath, J.R., 2011. The microscopic structure of adsorbed water on hydrophobic surfaces under ambient conditions, *Nano Letters*, 11 (12), 5581–5586.
- Cappa, C.D., Onasch, T.B., Massoli, P., Worsnop, D.R., Bates, T.S., Cross, E.S., Davidovits, P., Hakala, J., Hayden, K.L., and Jobson, B.T., 2012. Radiative absorption enhancements due to the mixing state of atmospheric black carbon, *Science*, 337 (6098), 1078–1081.
- Cappa, C.D., Onasch, T.B., Massoli, P., Worsnop, D.R., Bates, T.S., Cross, E.S., Davidovits, P., Hakala, J., Hayden, K.L., and Jobson, B.T., 2013. Response to comment on "radiative absorption enhancements due to the mixing state of atmospheric black carbon", *Science*, 339 (6118), 393–393.
- Cappa, C.D., Zhang, X., Russell, L.M., Collier, S., Lee, A.K.Y., Chen, C.L., Betha, R., Chen, S., Liu, J., Price, D.J., Sanchez, K.J., McMeeking, G.R., Williams, L.R., Onasch, T.B., Worsnop, D.R., Abbatt, J., and Zhang, Q., 2019. Light absorption by ambient black and brown carbon and its dependence on black carbon coating state for two california, USA, cities in winter and summer, *Journal of Geophysical Research: Atmospheres*, 124 (3), 1550–1577.
- Chamberlain, A., Clough, W., Heard, M.J., Newton, D., Stott, A.N.B., and Wells, A.C., 1975. Uptake of lead by inhalation of motor exhaust, *Proc. R. Soc. Lond. B*, 192, 192, 77–110.
- Chen, C., Enekwizu, O.Y., Fan, X., Dobrzanski, C.D., Ivanova, E.V., Ma, Y., Gor, G.Y., and Khalizov, A.F., 2018. Single parameter for predicting the morphology of atmospheric black carbon, *Environmental Science & Technology*, 52 (24), 14169–14179.
- Chen, C., Fan, X., Shaltout, T., Qiu, C., Ma, Y., Goldman, A., and Khalizov, A.F., 2016. An unexpected restructuring of combustion soot aggregates by subnanometer coatings of polycyclic aromatic hydrocarbons, *Geophys. Res. Lett.*, 43 (20), 11080–11088.

- Chen, D., Totton, T.S., Akroyd, J.W., Mosbach, S., and Kraft, M., 2014. Size-dependent melting of polycyclic aromatic hydrocarbon nano-clusters: A molecular dynamics study, *Carbon*, 67, 79–91.
- China, S., Kulkarni, G., Scarnato, B.V., Sharma, N., Pekour, M., Shilling, J.E., Wilson, J., Zelenyuk, A., Chand, D., Liu, S., Aiken, A.C., Dubey, M., Laskin, A., Zaveri, R.A., and Mazzoleni, C., 2015a. Morphology of diesel soot residuals from supercooled water droplets and ice crystals: implications for optical properties, *Environmental Research Letters*, 10 (11), 114010.
- China, S., Mazzoleni, C., Gorkowski, K., Aiken, A.C., and Dubey, M.K., 2013. Morphology and mixing state of individual freshly emitted wildfire carbonaceous particles, *Nat. Comm.*, 4, 4:2122.
- China, S., Salvadori, N., and Mazzoleni, C., 2014. Effect of traffic and driving characteristics on morphology of atmospheric soot particles at freeway on-ramps, *Environmental Science & Technology*, 48 (6), 3128–3135.
- China, S., Scarnato, B., Owen, R.C., Zhang, B., Ampadu, M.T., Kumar, S., Dzepina, K., Dziobak, M.P., Fialho, P., Perlinger, J.A., Hueber, J., Helmig, D., Mazzoleni, L.R., and Mazzoleni, C., 2015b. Morphology and mixing state of aged soot particles at a remote marine free troposphere site: Implications for optical properties, *Geophysical Research Letters*, 42 (4), 1243–1250.
- Christenson, H.K., 2001. Confinement effects on freezing and melting, *Journal of Physics: Condensed Matter*, 13 (11), R95–R133.
- Corbin, J., Lohmann, U., Sierau, B., Keller, A., Bartscher, H., and Mensah, A., 2015. Black carbon surface oxidation and organic composition of beech-wood soot aerosols, *Atmospheric Chemistry and Physics*, 15 (20), 11885–11907.
- Corbin, J.C., Czech, H., Massabò, D., de Mongeot, F.B., Jakobi, G., Liu, F., Lobo, P., Mennucci, C., Mensah, A.A., Orasche, J., Pieber, S.M., Prévôt, A.S.H., Stengel, B., Tay, L.L., Zannata, M., Zimmermann, R., Haddad, I.E., and Gysel, M., 2019. Infrared-absorbing carbonaceous tar can dominate light absorption by marine-engine exhaust, *npj Climate and Atmospheric Science*, 2 (1).
- Coz, E. and Leck, C., 2011. Morphology and state of mixture of atmospheric soot aggregates during the winter season over southern asia-a quantitative approach, *Tellus B: Chemical and Physical Meteorology*, 63 (1), 107–116.
- Crassous, J., Charlaix, E., and Loubet, J.L., 1994. Capillary condensation between high-energy surfaces. an experimental study with a surface force apparatus, *Europhysics Letters (EPL)*, 28 (1), 37–42.
- Cross, E.S., Onasch, T.B., Ahern, A., Wrobel, W., Slowik, J.G., Olfert, J., Lack, D.A., Massoli, P., Cappa, C.D., Schwarz, J.P., Spackman, J.R., Fahey, D.W., Sedlacek, A., Trimborn, A., Jayne, J.T., Freedman, A., Williams, L.R., Ng, N.L., Mazzoleni, C., Dubey, M., Brem, B., Kok, G., Subramanian, R., Freitag, S., Clarke, A., Thornhill, D., Marr, L.C., Kolb, C.E., Worsnop, D.R., and Davidovits, P., 2010. Soot particle studies—instrument inter-comparison—project overview, *Aerosol Sci. Technol.*, 44 (8), 592–611.
- Crouzet, Y. and Marlow, W.H., 1995. Calculations of the equilibrium vapor pressure of water over adhering 50–200-nm spheres, *Aerosol Science and Technology*, 22 (1), 43–59.
- David, R.O., Marcolli, C., Fahrni, J., Qiu, Y., Sirkin, Y.A.P., Molinero, V., Mahrt, F., Brühwiler, D., Lohmann, U., and Kanji, Z.A., 2019. Pore condensation and freezing is responsible for ice formation below water saturation for porous particles, *Proceedings of the National Academy of Sciences*, 116 (17), 8184–8189.
- DeCarlo, P., Slowik, J., Worsnop, D., Davidovits, P., and Jimenez, J., 2004. Particle morphology and density characterization by combined mobility and aerodynamic diameter measurements. part 1: Theory, *Aerosol Sci. Technol.*, 38, 1185–1205.
- Donahue, N.M., Trump, E.R., Pierce, J.R., and Riipinen, I., 2011. Theoretical constraints on pure vapor-pressure driven condensation of organics to ultrafine particles, *Geophysical Research Letters*, 38 (16), L16801.
- Dong, J., Zhao, J., and Liu, L., 2015. Morphological effects on the radiative properties of soot aerosols in different internally mixing states with sulfate, *Journal of Quantitative Spectroscopy and Radiative Transfer*, 165, 43–55.
- Ebert, M., Inerle-Hof, M., and Weinbruch, S., 2002. Environmental scanning electron microscopy as a new technique to determine the hygroscopic behaviour of individual aerosol particles, *Atmospheric Environment*, 36 (39-40), 5909–5916.
- Eggersdorfer, M.L. and Pratsinis, S.E., 2013. Agglomerates and aggregates of nanoparticles made in the gas phase, *Adv. Powder Technol.*
- Ehara, K., Hagwood, C., and Coakley, K.J., 1996. Novel method to classify aerosol particles according to their mass-to-charge ratio: aerosol particle mass analyser, *J. Aerosol Sci.*, 27 (2), 217–234.
- Enekwizu, O.Y., Hasani, A., and Khalizov, A.F., 2021. Vapor condensation and coating evaporation are both responsible for soot aggregate restructuring, *Environmental Science & Technology*, 55 (13), 8622–8630.
- Eral, H.B., 't Mannetje, D.J.C.M., and Oh, J.M., 2012. Contact angle hysteresis: a review of fundamentals and applications, *Colloid and Polymer Science*, 291 (2), 247–260.
- Fadeev, A.Y. and McCarthy, T.J., 1999. Trialkylsilane monolayers covalently attached to silicon surfaces: wettability studies indicating that molecular topography contributes to contact angle hysteresis, *Langmuir*, 15 (11), 3759–3766.

J.C. Corbin: Soot compacted by condensation or evaporation**19**

- Ferry, D., Suzanne, J., Nitsche, S., Popovitchewa, O.B., and Shonija, N.K., 2002. Water adsorption and dynamics on kerosene soot under atmospheric conditions, *Journal of Geophysical Research: Atmospheres*, 107 (D23), AAC 22–1–AAC 22–10.
- Fierce, L., Bond, T.C., Bauer, S.E., Mena, F., and Riemer, N., 2016. Black carbon absorption at the global scale is affected by particle-scale diversity in composition, *Nature Communications*, 7 (1).
- Fierce, L., Onasch, T.B., Cappa, C.D., Mazzoleni, C., China, S., Bhandari, J., Davidovits, P., Fischer, D.A., Helgestad, T., Lambe, A.T., Sedlacek, A.J., Smith, G.D., and Wolff, L., 2020. Radiative absorption enhancements by black carbon controlled by particle-to-particle heterogeneity in composition, *Proceedings of the National Academy of Sciences*, 117 (10), 5196–5203.
- Fierce, L., Riemer, N., and Bond, T.C., 2015. Explaining variance in black carbon's aging timescale, *Atmospheric Chemistry and Physics*, 15 (6), 3173–3191.
- Figueiredo, J.L., Pereira, M.F., Freitas, M.M., and Órfão, J.J., 1999. Modification of the surface chemistry of activated carbons, *Carbon*, 37 (9), 1379–1389.
- Forestieri, S.D., Helgestad, T.M., Lambe, A.T., Renbaum-Wolff, L., Lack, D.A., Massoli, P., Cross, E.S., Dubey, M.K., Mazzoleni, C., Olfert, J.S., III, A.J.S., Freedman, A., Davidovits, P., Onasch, T.B., and Cappa, C.D., 2018. Measurement and modeling of the multiwavelength optical properties of uncoated flame-generated soot, *Atmospheric Chemistry and Physics*, 18 (16), 12141–12159.
- Friedlander, S., 2000. *Smoke, Dust, and Haze: Fundamentals of Aerosol Dynamics*, Oxford, UK: Oxford University Press.
- Friedlander, S.K., Jang, H.D., and Ryu, K.H., 1998. Elastic behavior of nanoparticle chain aggregates, *Applied Physics Letters*, 72 (2), 173–175.
- Gao, K., Zhou, C.W., Meier, E.J.B., and Kanji, Z.A., 2022. Laboratory studies of ice nucleation onto bare and internally mixed soot–sulfuric acid particles, *Atmospheric Chemistry and Physics*, 22 (8), 5331–5364.
- Gao, L. and McCarthy, T.J., 2006. Contact angle hysteresis explained, *Langmuir*, 22 (14), 6234–6237.
- Ghazi, R. and Olfert, J., 2013. Coating mass dependence of soot aggregate restructuring due to coatings of oleic acid and dioctyl sebacate, *Aerosol Sci. Technol.*, 47 (2), 192–200.
- Guo, S., Hu, M., Lin, Y., Gomez-Hernandez, M., Zamora, M.L., Peng, J., Collins, D.R., and Zhang, R., 2016. OH-initiated oxidation of m-xylene on black carbon aging, *Environmental Science & Technology*, 50 (16), 8605–8612.
- Gysel, M., 2003. Properties of jet engine combustion particles during the PartEmis experiment: Hygroscopicity at subsaturated conditions, *Geophysical Research Letters*, 30 (11).
- Gysel, M., Laborde, M., Mensah, A.A., Corbin, J.C., Keller, A., Kim, J., Petzold, A., and Sierau, B., 2012. Technical note: The single particle soot photometer fails to reliably detect palas soot nanoparticles, *Atmos. Meas. Tech.*, 5.
- He, C., Li, Q., Liou, K.N., Qi, L., Tao, S., and Schwarz, J.P., 2016. Microphysics-based black carbon aging in a global CTM: constraints from HIPPO observations and implications for global black carbon budget, *Atmos. Chem. Phys.*, 16 (5), 3077–3098.
- Heinson, W.R., Liu, P., and Chakrabarty, R.K., 2016. Fractal scaling of coated soot aggregates, *Aerosol Sci. Technol.*, 51 (1), 12–19.
- Hu, K., Liu, D., Tian, P., Wu, Y., Deng, Z., Wu, Y., Zhao, D., Li, R., Sheng, J., Huang, M., Ding, D., Li, W., Wang, Y., and Wu, Y., 2021. Measurements of the diversity of shape and mixing state for ambient black carbon particles, *Geophysical Research Letters*, 48 (17).
- Hu, K., Liu, D., Tian, P., Wu, Y., Li, S., Zhao, D., Li, R., Sheng, J., Huang, M., Ding, D., Liu, Q., Jiang, X., Li, Q., and Tao, J., 2022. Identifying the fraction of core–shell black carbon particles in a complex mixture to constrain the absorption enhancement by coatings, *Environmental Science & Technology Letters*, 9 (4), 272–279.
- Huang, P.F., Turpin, B.J., Pihho, M.J., Kittelson, D.B., and McMurry, P.H., 1994. Effects of water condensation and evaporation on diesel chain-agglomerate morphology, *Journal of Aerosol Science*, 25 (3), 447–459.
- Ivanova, E.V., Khalizov, A.F., and Gor, G.Y., 2020. Kinetic model for competitive condensation of vapor between concave and convex surfaces in a soot aggregate, *Aerosol Science and Technology*, 55 (3), 302–315.
- Jacobson, M.Z., 2013. Comment on "radiative absorption enhancements due to the mixing state of atmospheric black carbon", *Science*, 339 (6118), 393–393.
- Järvinen, E., Ignatius, K., Nichman, L., Kristensen, T.B., Fuchs, C., Hoyle, C.R., Höppel, N., Corbin, J.C., Craven, J., Duplissy, J., Ehrhart, S., Haddad, I.E., Frege, C., Gordon, H., Jokinen, T., Kallinger, P., Kirkby, J., Kiselev, A., Naumann, K.H., Petäjä, T., Pinterich, T., Prevot, A.S.H., Saathoff, H., Schiebel, T., Sengupta, K., Simon, M., Slowik, J.G., Tröstl, J., Virtanen, A., Vochezer, P., Vogt, S., Wagner, A.C., Wagner, R., Williamson, C., Winkler, P.M., Yan, C., Baltensperger, U., Donahue, N.M., Flagan, R.C., Gallagher, M., Hansel, A., Kulmala, M., Stratmann, F., Worsnop, D.R., Möhler, O., Leisner, T., and Schnaiter, M., 2016. Observation of viscosity transition in α -pinene secondary organic aerosol, *Atmospheric Chemistry and Physics*, 16 (7), 4423–4438.

- Jennings, S.G., 1988. The mean free path in air, *J. Aerosol Sci.*, 19 (2), 159–166.
- Johnson, K.S., Zuberi, B., Molina, L., Molina, M.J., Iedema, M.J., Cowin, J.P., Gaspar, D.J., Wang, C., and Laskin, A., 2005. Processing of soot in an urban environment: case study from the Mexico City metropolitan area, *Atmos. Chem. Phys.*, 5 (11), 3033–3043.
- Kahnert, M., 2017. Optical properties of black carbon aerosols encapsulated in a shell of sulfate: comparison of the closed cell model with a coated aggregate model, *Opt. Express*, 25 (20), 24579.
- Kanngießer, F. and Kahnert, M., 2018. Calculation of optical properties of light-absorbing carbon with weakly absorbing coating: A model with tunable transition from film-coating to spherical-shell coating, *Journal of Quantitative Spectroscopy and Radiative Transfer*, 216, 17–36.
- Kelesidis, G.A., Furrer, F.M., Wegner, K., and Pratsinis, S.E., 2018. Impact of humidity on silica nanoparticle agglomerate morphology and size distribution, *Langmuir*, 34 (29), 8532–8541.
- Kelesidis, G.A., Neubauer, D., Fan, L.S., Lohmann, U., and Pratsinis, S.E., 2022. Enhanced light absorption and radiative forcing by black carbon agglomerates, *Environmental Science & Technology*, 56 (12), 8610–8618.
- Kelesidis, G.A. and Pratsinis, S.E., 2019. Estimating the internal and surface oxidation of soot agglomerates, *Combustion and Flame*, 209, 493–499.
- Khalizov, A.F., Lin, Y., Qiu, C., Guo, S., Collins, D., and Zhang, R., 2013. Role of OH-initiated oxidation of isoprene in aging of combustion soot, *Environmental Science & Technology*, 47 (5), 2254–2263.
- Khalizov, A.F., Zhang, R., Zhang, D., Xue, H., Pagels, J., and McMurry, P.H., 2009. Formation of highly hygroscopic soot aerosols upon internal mixing with sulfuric acid vapor, *J. Geophys. Res.*, 114 (D5).
- Kleinwechter, H., Friedlander, S., and Schmidt-Ott, A., 1997. Investigation of agglomerate restructuring, *Journal of Aerosol Science*, 28, S763–S764.
- Köllensperger, G., Friedbacher, G., Kotzick, R., Niessner, R., and Grasserbauer, M., 1999. In-situ investigation of aerosol particles by atomic force microscopy, *Fresenius' J Anal Chem*, 361 (6-7), 716–721.
- Kohonen, M.M., Maeda, N., and Christenson, H.K., 1999. Kinetics of capillary condensation in a nanoscale pore, *Physical Review Letters*, 82 (23), 4667–4670.
- Koop, T., Bookhold, J., Shiraiwa, M., and Pöschl, U., 2011. Glass transition and phase state of organic compounds: dependency on molecular properties and implications for secondary organic aerosols in the atmosphere, *Physical Chemistry Chemical Physics*, 13 (43), 19238.
- Kütz, S. and Schmidt-Ott, A., 1992. Characterization of agglomerates by condensation-induced restructuring, *J. Aerosol Sci.*, 23, 357–360.
- Laaksonen, A., 2015. A unifying model for adsorption and nucleation of vapors on solid surfaces, *The Journal of Physical Chemistry A*, 119 (16), 3736–3745.
- Laaksonen, A., Malila, J., and Nenes, A., 2020. Heterogeneous nucleation of water vapor on different types of black carbon particles.
- Laborde, M., Mertes, P., Zieger, P., Dommen, J., Baltensperger, U., and Gysel, M., 2012. Sensitivity of the single particle soot photometer to different black carbon types, *Atmos. Meas. Tech.*, 5, 1031–1043.
- Lack, D.A., Langridge, J.M., Bahreini, R., Cappa, C.D., Middlebrook, A.M., and Schwarz, J.P., 2012. Brown carbon and internal mixing in biomass burning particles, *Proceedings of the National Academy of Sciences*, 109 (37), 14802–14807.
- Lamb, D. and Verlinde, J., 2011. *Physics and chemistry of clouds*, Cambridge, UK: Cambridge University Press.
- Lauga, E. and Brenner, M.P., 2004. Evaporation-driven assembly of colloidal particles, *Phys. Rev. Lett.*, 93 (23).
- Lefevre, G., Yon, J., Bouvier, M., Liu, F., and Coppalle, A., 2019. Impact of organic coating on soot angular and spectral scattering properties, *Environmental Science & Technology*, 53 (11), 6383–6391.
- Leung, K.K., Schnitzler, E.G., Dastanpour, R., Rogak, S.N., Jäger, W., and Olfert, J.S., 2017a. Relationship between coating-induced soot aggregate restructuring and primary particle number, *Environmental Science & Technology*, 51 (15), 8376–8383.
- Leung, K.K., Schnitzler, E.G., Jäger, W., and Olfert, J.S., 2017b. Relative humidity dependence of soot aggregate restructuring induced by secondary organic aerosol: Effects of water on coating viscosity and surface tension, *Environ. Sci. Technol. Lett.*
- Li, Y.J., Liu, P., Gong, Z., Wang, Y., Bateman, A.P., Bergoend, C., Bertram, A.K., and Martin, S.T., 2015. Chemical reactivity and liquid/nonliquid states of secondary organic material, *Environmental Science & Technology*, 49 (22), 13264–13274.
- Lieke, K.I., Rosenørn, T., Pedersen, J., Larsson, D., Kling, J., Fuglsang, K., and Bilde, M., 2013. Micro- and nanostructural characteristics of particles before and after an exhaust gas recirculation system scrubber, *Aerosol Science and Technology*, 47 (9), 1038–1046.
- Liu, F., Yon, J., and Bescond, A., 2016. On the radiative properties of soot aggregates – part 2: Effects of coating, *Journal of Quantitative Spectroscopy and Radiative Transfer*, 172, 134–145.

J.C. Corbin: Soot compacted by condensation or evaporation**21**

- Liu, L. and Mishchenko, M., 2018. Scattering and radiative properties of morphologically complex carbonaceous aerosols: A systematic modeling study, *Remote Sensing*, 10 (10), 1634.
- Lopatkin, Y.M., Protsenko, I.E., and Skorobogatko, A.F., 1977. Structure of anthracene thin films, *Krist. Tech.*, 12 (9), 903–905.
- Luo, J., Zhang, Q., Zhang, C., Zhang, Y., and Chakrabarty, R.K., 2021. The fractal characteristics of atmospheric coated soot: Implication for morphological analysis, *Journal of Aerosol Science*, 157, 105804.
- Luo, J., Zhang, Y., Wang, F., and Zhang, Q., 2018. Effects of brown coatings on the absorption enhancement of black carbon: a numerical investigation, *Atmospheric Chemistry and Physics*, 18 (23), 16897–16914.
- Luo, J., Zhang, Y., and Zhang, Q., 2020. The ångström exponent and single-scattering albedo of black carbon: Effects of different coating materials, 11 (10), 1103.
- Ma, X., Zangmeister, C.D., Gigault, J., Mulholland, G.W., and Zachariah, M.R., 2013a. Soot aggregate restructuring during water processing, *J. Aerosol Sci.*
- Ma, X., Zangmeister, C.D., and Zachariah, M.R., 2013b. Soot oxidation kinetics: A comparison study of two tandem ion-mobility methods, *The Journal of Physical Chemistry C*, 117 (20), 10723–10729.
- Manoharan, V.N., 2003. Dense packing and symmetry in small clusters of microspheres, *Science*, 301 (5632), 483–487.
- Marcolli, C., 2014. Deposition nucleation viewed as homogeneous or immersion freezing in pores and cavities, *Atmos. Chem. Phys.*, 14 (4), 2071–2104.
- Marcolli, C., Luo, B., and Peter, T., 2004. Mixing of the organic aerosol fractions: liquids as the thermodynamically stable phases, *The Journal of Physical Chemistry A*, 108 (12), 2216–2224.
- Maricq, M.M., 2014. Examining the relationship between black carbon and soot in flames and engine exhaust, *Aerosol Sci. Technol.*, 48 (6), 620–629.
- Matuschek, G., Karg, E., Schröppel, A., Schulz, H., and Schmid, O., 2007. Chemical investigation of eight different types of carbonaceous particles using thermoanalytical techniques, *Environ. Sci. Technol.*, 41 (24), 8406–8411.
- Mikhailov, E., Vlasenko, S., Kiselev, A., and Ryshkevich, T., 1997. The structural changes in fractal particles of carbon black under the effect of capillary forces: Experimental results, *Colloid Journal of the Russian Academy of Sciences: Kolloidnyi Zhurnal*, 59 (2), 176–184.
- Mikhailov, E., Vlasenko, S., Podgorny, I., Ramanathan, V., and Corrigan, C., 2006. Optical properties of soot–water drop agglomerates: An experimental study, *J. Geophys. Res.*, 111 (D7), D07209.
- Miljevic, B., Heringa, M., Keller, A., Meyer, N., Good, J., Lauber, A., Decarlo, P., Fairfull-Smith, K., Nussbaumer, T., and Burtscher, H., 2010. Oxidative potential of logwood and pellet burning particles assessed by a novel profluorescent nitroxide probe, *Environ. Sci. Technol.*, 44 (17), 6601–6607.
- Moteki, N. and Kondo, Y., 2007. Effects of mixing state on black carbon measurements by laser-induced incandescence, *Aerosol Sci. Technol.*, 41 (4), 398–417.
- Moteki, N., Kondo, Y., and Adachi, K., 2014. Identification by single-particle soot photometer of black carbon particles attached to other particles: Laboratory experiments and ground observations in tokyo, *Journal of Geophysical Research: Atmospheres*, 119 (2), 1031–1043.
- Nanda, K.K., 2009. Size-dependent melting of nanoparticles: Hundred years of thermodynamic model, *Pramana - J Phys*, 72 (4), 617–628.
- Narhe, R.D. and Beysens, D.A., 2004. Nucleation and growth on a superhydrophobic grooved surface, *Physical Review Letters*, 93 (7).
- Narhe, R.D. and Beysens, D.A., 2006. Water condensation on a super-hydrophobic spike surface, *Europhysics Letters (EPL)*, 75 (1), 98–104.
- Nemes-Incze, P., Osváth, Z., Kamarás, K., and Biró, L., 2008. Anomalies in thickness measurements of graphene and few layer graphite crystals by tapping mode atomic force microscopy, *Carbon*, 46 (11), 1435–1442.
- Nguyen, H.V., Okuyama, K., Mimura, T., Kousaka, Y., Flagan, R.C., and Seinfeld, J.H., 1987. Homogeneous and heterogeneous nucleation in a laminar flow aerosol generator, *Journal of Colloid and Interface Science*, 119 (2), 491–504.
- Niemi, J.V., Saarikoski, S., Tervahattu, H., Mäkelä, T., Hillamo, R., Vehkamäki, H., Sogacheva, L., and Kulmala, M., 2006. Changes in background aerosol composition in finland during polluted and clean periods studied by tem/edx individual particle analysis, *Atmos. Chem. Phys.*, 6 (12), 5049–5066.
- Olfert, J. and Rogak, S., 2019. Universal relations between soot effective density and primary particle size for common combustion sources, *Aerosol Science and Technology*, 53 (5), 485–492.
- Ouf, F.X., Bourrous, S., Fauvel, S., Kort, A., Lintis, L., Nuvoli, J., and Yon, J., 2019. True density of combustion emitted particles: A comparison of results highlighting the influence of the organic contents, *Journal of Aerosol Science*, 134, 1–13.

- Pagels, J., Khalizov, A.F., McMurry, P.H., and Zhang, R.Y., 2009. Processing of soot by controlled sulphuric acid and water condensation—mass and mobility relationship, *Aerosol Sci. Technol.*, 43 (7), 629–640.
- Pawlow, P., 1909. Über die abhängigkeit des schmelzpunktes von der oberflächenenergie eines festen körpers, *Z. phys. Chem*, 65, 1–35.
- Pei, X., Hallquist, M., Eriksson, A.C., Pagels, J., Donahue, N.M., Mentel, T., Svenningsson, B., Brune, W., and Pathak, R.K., 2018. Morphological transformation of soot: investigation of microphysical processes during the condensation of sulfuric acid and limonene ozonolysis product vapors, *Atmospheric Chemistry and Physics*, 18 (13), 9845–9860.
- Peng, J., Hu, M., Guo, S., Du, Z., Zheng, J., Shang, D., Zamora, M.L., Zeng, L., Shao, M., Wu, Y.S., Zheng, J., Wang, Y., Glen, C.R., Collins, D.R., Molina, M.J., and Zhang, R., 2016. Markedly enhanced absorption and direct radiative forcing of black carbon under polluted urban environments, *Proceedings of the National Academy of Sciences*, 113 (16), 4266–4271.
- Persiantseva, N.M., Popovicheva, O.B., and Shonija, N.K., 2004. Wetting and hydration of insoluble soot particles in the upper troposphere, *J. Environ. Monit.*, 6 (12), 939.
- Peters, C.A., Mukherji, S., Knightes, C.D., and Weber, W.J., 1997. Phase stability of multicomponent NAPLs containing PAHs, *Environmental Science & Technology*, 31 (9), 2540–2546.
- Pitois, O., Moucheron, P., and Chateau, X., 2000. Liquid bridge between two moving spheres: An experimental study of viscosity effects, *Journal of Colloid and Interface Science*, 231 (1), 26–31.
- Qiu, C., Khalizov, A.F., and Zhang, R., 2012. Soot aging from OH-initiated oxidation of toluene, *Environmental Science & Technology*, 46 (17), 9464–9472.
- Radney, J.G., You, R., Ma, X., Conny, J.M., Zachariah, M.R., Hodges, J.T., and Zangmeister, C.D., 2014. Dependence of soot optical properties on particle morphology: Measurements and model comparisons, *Environ. Sci. Technol.*, 48 (6), 3169–3176.
- Ramanathan, V. and Carmichael, G., 2008. Global and regional climate changes due to black carbon, *Nat. Geosci.*, 1 (4), 221–227.
- Restagno, F., Bocquet, L., and Biben, T., 2000. Metastability and nucleation in capillary condensation, *Physical Review Letters*, 84 (11), 2433–2436.
- Riemer, N., Vogel, H., and Vogel, B., 2004. Soot aging time scales in polluted regions during day and night, *Atmospheric Chemistry and Physics*, 4 (7), 1885–1893.
- Rissler, J., Messing, M.E., Malik, A.I., Nilsson, P.T., Nordin, E.Z., Bohgard, M., Sanati, M., and Pagels, J.H., 2013. Effective density characterization of soot agglomerates from various sources and comparison to aggregation theory, *Aerosol Science and Technology*, 47 (7), 792–805.
- Rissler, J., Swietlicki, E., Bengtsson, A., Boman, C., Pagels, J., Sandström, T., Blomberg, A., and Löndahl, J., 2012. Experimental determination of deposition of diesel exhaust particles in the human respiratory tract, *Journal of Aerosol Science*, 48, 18–33.
- Rocca, A.L., Liberto, G.D., Shayler, P., and Fay, M., 2013. The nanostructure of soot-in-oil particles and agglomerates from an automotive diesel engine, *Tribology International*, 61, 80–87.
- Romshoo, B., Müller, T., Pfeifer, S., Saturno, J., Nowak, A., Ciupek, K., Quincey, P., and Wiedensohler, A., 2021. Radiative properties of coated black carbon aggregates: numerical simulations and radiative forcing estimates.
- Roux, M.V., Temprado, M., Chickos, J.S., and Nagano, Y., 2008. Critically evaluated thermochemical properties of polycyclic aromatic hydrocarbons, *Journal of Physical and Chemical Reference Data*, 37 (4), 1855–1996.
- Scarnato, B., Vahidinia, S., Richard, D., and Kirchstetter, T., 2013. Effects of internal mixing and aggregate morphology on optical properties of black carbon using a discrete dipole approximation model, *Atmos. Chem. Phys.*, 13 (10), 5089–5101.
- Scheckman, J.H. and McMurry, P.H., 2011. Deposition of silica agglomerates in a cast of human lung airways: Enhancement relative to spheres of equal mobility and aerodynamic diameter, *J. Aerosol Sci.*, 42 (8), 508–516.
- Schäffer, E. and Wong, P., 2000. Contact line dynamics near the pinning threshold: A capillary rise and fall experiment, *Physical Review E*, 61 (5), 5257–5277.
- Schmale, J., Henning, S., Decesari, S., Henzing, B., Keskinen, H., Sellegri, K., Ovadnevaite, J., Pöhlker, M.L., Brito, J., Bougiatioti, A., Kristensson, A., Kalivitis, N., Stavroulas, I., Carbone, S., Jefferson, A., Park, M., Schlag, P., Iwamoto, Y., Aalto, P., Äijälä, M., Bukowiecki, N., Ehn, M., Frank, G., Fröhlich, R., Frumau, A., Herrmann, E., Herrmann, H., Holzinger, R., Kos, G., Kulmala, M., Mihalopoulos, N., Nenes, A., O'Dowd, C., Petäjä, T., Picard, D., Pöhlker, C., Pöschl, U., Poulain, L., Prévôt, A.S.H., Swietlicki, E., Andreae, M.O., Artaxo, P., Wiedensohler, A., Ogren, J., Matsuki, A., Yum, S.S., Stratmann, F., Baltensperger, U., and Gysel, M., 2018. Long-term cloud condensation nuclei number concentration, particle number size distribution and chemical composition measurements at regionally representative observatories, *Atmospheric Chemistry and Physics*, 18 (4), 2853–2881.

- Schmedding, R., Rasool, Q.Z., Zhang, Y., Pye, H.O.T., Zhang, H., Chen, Y., Surratt, J.D., Lopez-Hilfiker, F.D., Thornton, J.A., Goldstein, A.H., and Vizuete, W., 2020. Predicting secondary organic aerosol phase state and viscosity and its effect on multiphase chemistry in a regional-scale air quality model, *Atmospheric Chemistry and Physics*, 20 (13), 8201–8225.
- Schmidt, M., Kusche, R., von Issendorff, B., and Haberland, H., 1998. Irregular variations in the melting point of size-selected atomic clusters, *Nature*, 393 (6682), 238–240.
- Schmidt-Ott, A., 1988. New approaches to in situ characterization of ultrafine agglomerates, *Journal of Aerosol Science*, 19 (5), 553–563.
- Schnitzler, E.G., Dutt, A., Charbonneau, A.M., Olfert, J.S., and Jäger, W., 2014. Soot aggregate restructuring due to coatings of secondary organic aerosol derived from aromatic precursors, *Environ. Sci. Technol.*, 48 (24), 14309–14316.
- Schnitzler, E.G., Gac, J.M., and Jäger, W., 2017. Coating surface tension dependence of soot aggregate restructuring, *J. Aerosol Sci.*, 106, 43–55.
- Schwarz, J.P., Gao, R.S., Fahey, D.W., Thomson, D.S., Watts, L.A., Wilson, J.C., Reeves, J.M., Darbeheshti, M., Baumgardner, D.G., Kok, G.L., Chung, S.H., Schulz, M., Hendricks, J., Lauer, A., Kärcher, B., Slowik, J.G., Rosenlof, K.H., Thompson, T.L., Langford, A.O., Loewenstein, M., and Aikin, K.C., 2006. Single-particle measurements of midlatitude black carbon and light-scattering aerosols from the boundary layer to the lower stratosphere, *J. Geophys. Res.*, 111, D16207.
- Shi, Z., Shao, L., Jones, T., Whittaker, A., Lu, S., Bérubé, K., He, T., and Richards, R., 2003. Characterization of airborne individual particles collected in an urban area, a satellite city and a clean air area in Beijing, 2001, *Atmospheric Environment*, 37 (29), 4097–4108.
- Shi, Z., Zhang, Y., Liu, M., Hanaor, D.A., and Gan, Y., 2018. Dynamic contact angle hysteresis in liquid bridges, *Colloids and Surfaces A: Physicochemical and Engineering Aspects*, 555, 365–371.
- Shrivastava, M., Cappa, C.D., Fan, J., Goldstein, A.H., Guenther, A.B., Jimenez, J.L., Kuang, C., Laskin, A., Martin, S.T., Ng, N.L., Petaja, T., Pierce, J.R., Rasch, P.J., Roldin, P., Seinfeld, J.H., Shilling, J., Smith, J.N., Thornton, J.A., Volkamer, R., Wang, J., Worsnop, D.R., Zaveri, R.A., Zelenyuk, A., and Zhang, Q., 2017. Recent advances in understanding secondary organic aerosol: Implications for global climate forcing, *Reviews of Geophysics*, 55 (2), 509–559.
- Slowik, J.G., Cross, E.S., Han, J.H., Kolucki, J., Davidovits, P., Williams, L.R., Onasch, T.B., Jayne, J.T., Kolb, C.E., and Worsnop, D.R., 2007. Measurements of morphology changes of fractal soot particles using coating and denuding experiments: Implications for optical absorption and atmospheric lifetime, *Aerosol Sci. Technol.*, 41 (8), 734–750.
- Song, M., Liu, P.F., Hanna, S.J., Zaveri, R.A., Potter, K., You, Y., Martin, S.T., and Bertram, A.K., 2016. Relative humidity-dependent viscosity of secondary organic material from toluene photo-oxidation and possible implications for organic particulate matter over megacities, *Atmospheric Chemistry and Physics*, 16 (14), 8817–8830.
- Sorensen, C., 2011. The mobility of fractal aggregates: a review, *Aerosol Sci. Technol.*, 45 (7), 765–779.
- Tajima, N., Fukushima, N., Ehara, K., and Sakurai, H., 2011. Mass range and optimized operation of the aerosol particle mass analyzer, *Aerosol Sci. Technol.*, 45 (2), 196–214.
- Toth, P., Jacobsson, D., Ek, M., and Wiinikka, H., 2019. Real-time, in situ, atomic scale observation of soot oxidation, *Carbon*, 145, 149–160.
- Tritscher, T., Jurányi, Z., Martin, M., Chirico, R., Gysel, M., Heringa, M.F., DeCarlo, P.F., Sierau, B., Prévôt, A.S.H., and Weingartner, E., 2011. Changes of hygroscopicity and morphology during ageing of diesel soot, *Environ. Res. Lett.*, 6 (3), 034026.
- Tröstl, J., Chuang, W.K., Gordon, H., Heinritzi, M., Yan, C., Molteni, U., Ahlm, L., Frege, C., Bianchi, F., Wagner, R., Simon, M., Lehtipalo, K., Williamson, C., Craven, J.S., Duplissy, J., Adamov, A., Almeida, J., Bernhammer, A.K., Breitenlechner, M., Brilke, S., Dias, A., Ehrhart, S., Flagan, R.C., Franchin, A., Fuchs, C., Guida, R., Gysel, M., Hansel, A., Hoyle, C.R., Jokinen, T., Junninen, H., Kangasluoma, J., Keskinen, H., Kim, J., Krapf, M., Kürten, A., Laaksonen, A., Lawler, M., Leiminger, M., Mathot, S., Möhler, O., Nieminen, T., Onnela, A., Petäjä, T., Piel, F.M., Miettinen, P., Rissanen, M.P., Rondo, L., Sarnela, N., Schobesberger, S., Sengupta, K., Sipilä, M., Smith, J.N., Steiner, G., Tomè, A., Virtanen, A., Wagner, A.C., Weingartner, E., Wimmer, D., Winkler, P.M., Ye, P., Carslaw, K.S., Curtius, J., Dommen, J., Kirkby, J., Kulmala, M., Riipinen, I., Worsnop, D.R., Donahue, N.M., and Baltensperger, U., 2016. The role of low-volatility organic compounds in initial particle growth in the atmosphere, *Nature*, 533 (7604), 527–531.
- Vakkari, V., Kerminen, V.M., Beukes, J.P., Tiitta, P., Zyl, P.G., Josipovic, M., Venter, A.D., Jaars, K., Worsnop, D.R., Kulmala, M., and Laakso, L., 2014. Rapid changes in biomass burning aerosols by atmospheric oxidation, *Geophys. Res. Lett.*, 41 (7), 2644–2651.
- Wang, Y., Liu, F., He, C., Bi, L., Cheng, T., Wang, Z., Zhang, H., Zhang, X., Shi, Z., and Li, W., 2017. Fractal dimensions and mixing structures of soot particles during atmospheric processing, *Environmental Science & Technology Letters*, 4 (11), 487–493.
- Weingartner, E., Baltensperger, U., and Burtscher, H., 1995. Growth and structural change of combustion aerosols at high relative humidity, *Environ. Sci. Technol.*, 29 (12), 2982–2986.

- Weingartner, E., Burtscher, H., and Baltensperger, U., 1997. Hygroscopic properties of carbon and diesel soot particles, *Atmospheric Environment*, 31 (15), 2311–2327.
- Worringen, A., Ebert, M., Trautmann, T., Weinbruch, S., and Helas, G., 2008. Optical properties of internally mixed ammonium sulfate and soot particles—a study of individual aerosol particles and ambient aerosol populations, *Applied Optics*, 47 (21), 3835.
- Wu, Y., Cheng, T., Zheng, L., and Chen, H., 2016. Models for the optical simulations of fractal aggregated soot particles thinly coated with non-absorbing aerosols, *Journal of Quantitative Spectroscopy and Radiative Transfer*, 182, 1–11.
- Wu, Y., Cheng, T., Zheng, L., and Chen, H., 2017. Sensitivity of mixing states on optical properties of fresh secondary organic carbon aerosols, *Journal of Quantitative Spectroscopy and Radiative Transfer*, 195, 147–155.
- Xiong, C. and Friedlander, S.K., 2001. Morphological properties of atmospheric aerosol aggregates, *Proceedings of the National Academy of Sciences*, 98 (21), 11851–11856.
- Xu, K., Cao, P., and Heath, J.R., 2010. Graphene visualizes the first water adlayers on mica at ambient conditions, *Science*, 329 (5996), 1188–1191.
- Xue, H., Khalizov, A.F., Wang, L., Zheng, J., and Zhang, R., 2009. Effects of coating of dicarboxylic acids on the mass-mobility relationship of soot particles, *Environ. Sci. Technol.*, 43 (8), 2787–2792.
- Yon, J., Liu, F., Bescond, A., Caumont-Prim, C., Rozé, C., Ouf, F.X., and Coppalle, A., 2014. Effects of multiple scattering on radiative properties of soot fractal aggregates, *J. Quant. Spectrosc. Radiat. Transfer*, 133, 374–381.
- Yuan, J., Modini, R.L., Zanatta, M., Herber, A.B., Müller, T., Wehner, B., Poulain, L., Tuch, T., Baltensperger, U., and Gysel-Beer, M., 2021. Variability in the mass absorption cross section of black carbon (BC) aerosols is driven by BC internal mixing state at a central european background site (melpitz, germany) in winter, *Atmospheric Chemistry and Physics*, 21 (2), 635–655.
- Zangmeister, C.D., Radney, J.G., Dockery, L.T., Young, J.T., Ma, X., You, R., and Zachariah, M.R., 2014. Packing density of rigid aggregates is independent of scale, *Proceedings of the National Academy of Sciences*, 111 (25), 9037–9041.
- Zelenay, V., Mooser, R., Tritscher, T., Kvrepelová, A., Heringa, M., Chirico, R., Prévôt, A., Weingartner, E., Baltensperger, U., and Dommen, J., 2011. Aging induced changes on nexafs fingerprints in individual combustion particles, *Atmos. Chem. Phys.*, 11 (22), 11777–11791.
- Zhang, R., Khalizov, A.F., Pagels, J., Zhang, D., Xue, H., and McMurry, P.H., 2008. Variability in morphology, hygroscopicity, and optical properties of soot aerosols during atmospheric processing, *Proc. Natl. Acad. Sci. U.S.A.*, 105 (30), 10291–10296.
- Zhang, Y., Favez, O., Canonaco, F., Liu, D., Močnik, G., Amodeo, T., Sciare, J., Prévôt, A.S.H., Gros, V., and Albinet, A., 2018. Evidence of major secondary organic aerosol contribution to lensing effect black carbon absorption enhancement, *npj Climate and Atmospheric Science*, 1 (1).
- Zheng, L. and Wu, Y., 2021. Effects of primary particle size on light absorption enhancement of black carbon aerosols using the superposition t-matrix method, *Journal of Quantitative Spectroscopy and Radiative Transfer*, 258, 107388.
- Zuberi, B., Johnson, K.S., Aleks, G.K., Molina, L.T., Molina, M.J., and Laskin, A., 2005. Hydrophilic properties of aged soot, *Geophys. Res. Lett.*, 32 (1), L01807.

Table 1. Summary of coating addition/removal pathways and their corresponding compaction mechanisms. Mechanisms are defined in Figure 1 and Section 2. Pathways are explained in Figure 2 and Section 4.1. Figures 3–5 illustrate the results of following these pathways.

θ [°]	Pathway ^a	Coating phase upon addition—removal	Compaction mechanisms ^b	Material used in this study
n.a. ^c	SS	Solid—Solid	—	Anthracene
< 90	SL	Solid—Liquid	DEC	Anthracene
< 90	LS	Liquid—Solid	CC	Anthracene
< 90	LL	Liquid—Liquid	CC and DEC	Oleic acid
> 90	NL	Liquid (nanodroplet)—Liquid	NDA and DEC	n.a.

^aFirst and second letters represent the added and removed phases, respectively. ^bFor definitions see Figure 1. ^cn.a. = not applicable.

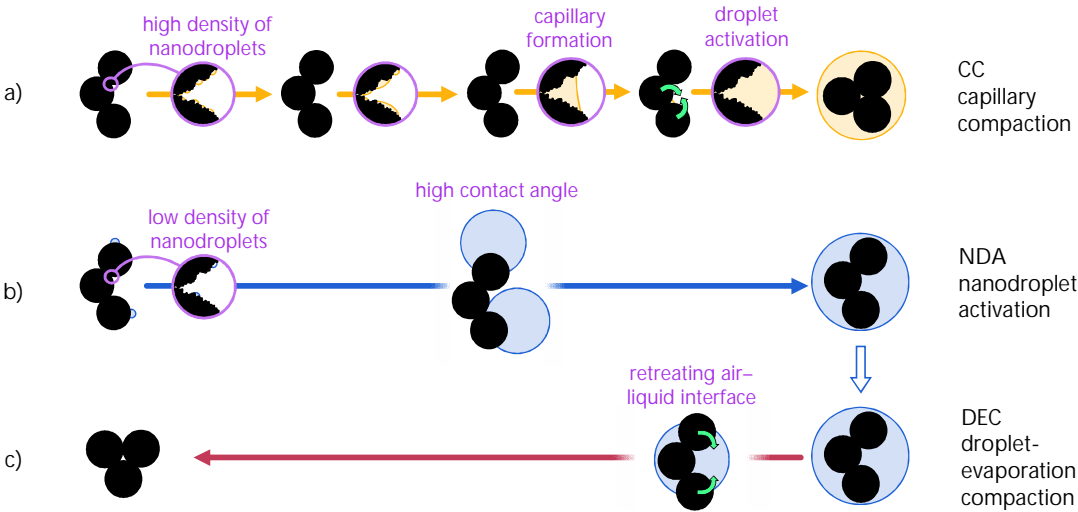


Figure 1. Compaction mechanisms for soot in the context of the activation barriers (inset circles) involved in forming the liquid phase. These mechanisms are based on the experimental observations reviewed in Section 2 and are generally sensitive to both time (kinetic limitations) and vapour saturation (thermodynamic limitations). Yellow and blue colours indicate liquids with low and high contact angles, respectively. Dark-red arrows indicate evaporation, which is only depicted for the case where compaction was avoided during condensation. Green curved arrows show torque due to compaction forces. In the inset circles, surface heterogeneities that may act as adsorption sites are depicted by the jagged line. For NDA, the critical droplet diameter prior to activation is drawn at a scale that represents an approximate critical diameter, assuming a 30 nm diameter soot spherule.

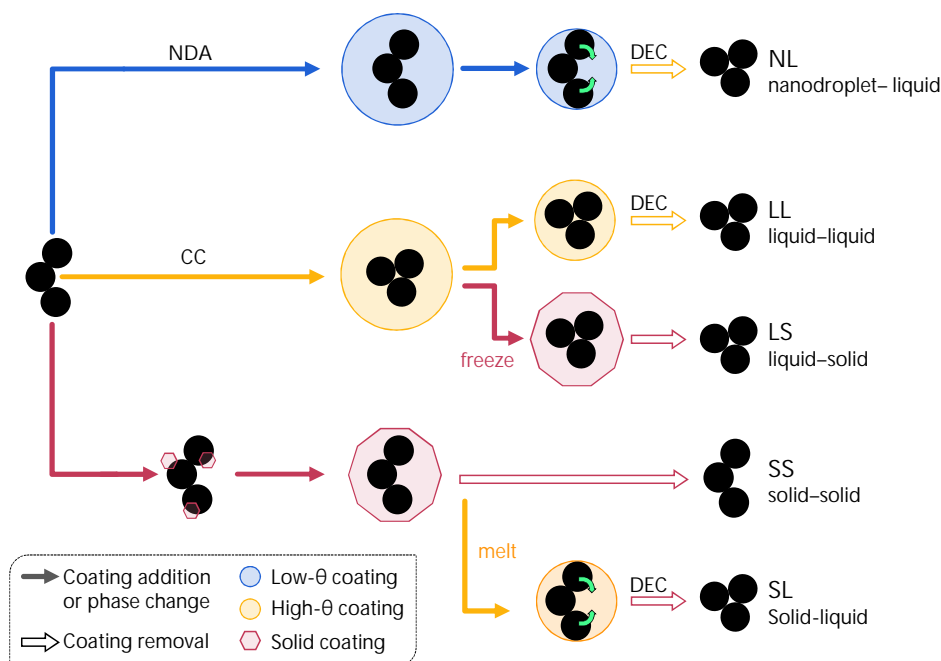


Figure 2. Experimental pathways towards soot compaction by condensation or evaporation. This figure illustrates how the mechanisms defined in Table 1 and illustrated in Figure 1 can be explored by adding and removing solid (“S”) and liquid (“L”) coatings. Blue and red arrows indicate liquid and solid phase coatings, respectively. Solid arrows indicate coating addition or phase transformation, open arrows coating removal. Red, blue, and orange coatings indicate solid, low- θ liquid, and high- θ liquid phases, respectively. Green arrows indicate opportunities for compaction (mechanisms shown in Figure 1). In our experiments, the nanodroplet-liquid (NL) pathway was not achieved due to the low contact angles between our coating materials (oleic acid and anthracene) with soot.

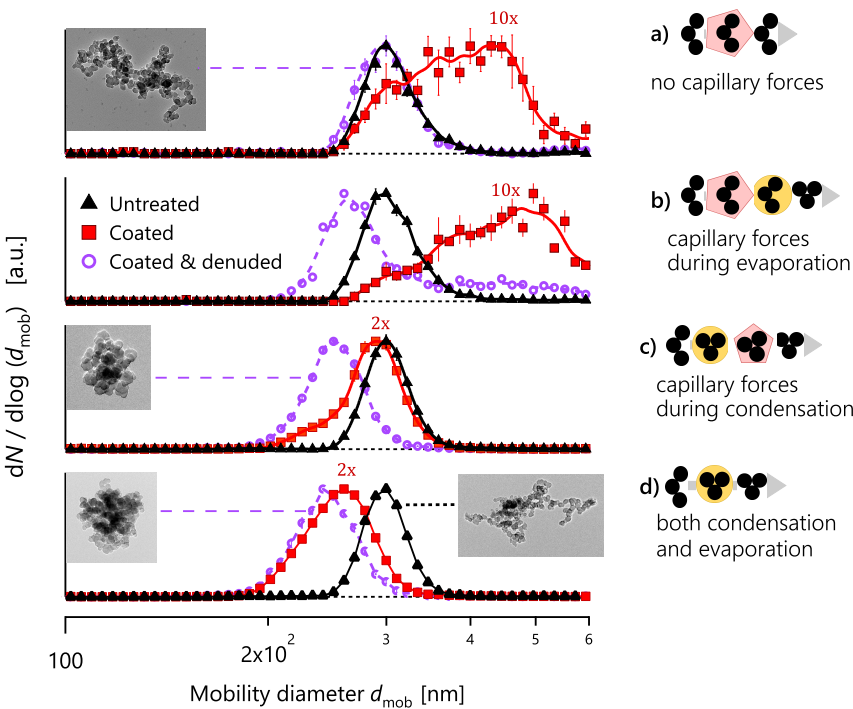


Figure 3. Normalized size distributions of 300 nm soot particles without treatment (\blacktriangle), after addition of solid or liquid organic coatings (\blacksquare), and after removal of coatings (\circ). The four panels correspond to different coating phases on addition or removal, which allows different compaction mechanisms (Table 1 and Figure 1) to proceed. Panels (a) shows that neither deposition nor sublimation causes compaction. Panels (b) shows that condensation alone caused compaction. Panel (c) shows that evaporation alone caused compaction. Panel (d) shows the result of both condensation and evaporation compaction. Some curves are labelled with exemplary TEM images (soot monomer diameters 30 ± 6 nm) of coated–denuded or untreated samples. The numbers above the coated data points give the volume growth factors (2x, 10x) for comparison with Figure 4.

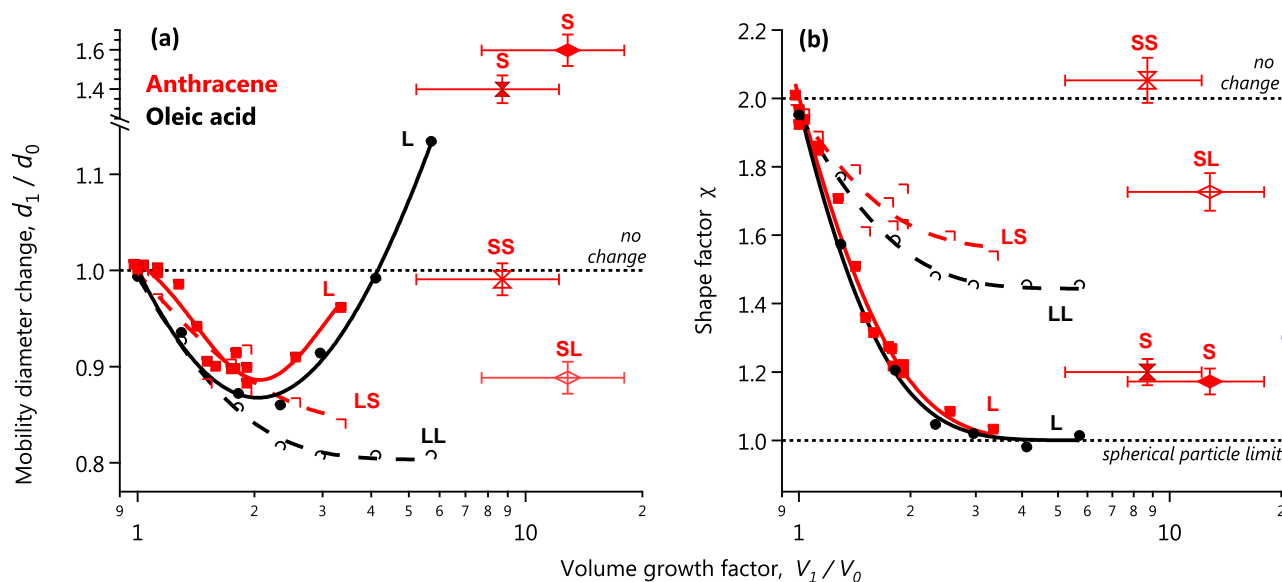


Figure 4. (a) Change in mobility diameter relative to its initial value, d_1/d_0 , and (b) shape factor χ of 300 nm soot as a function of coating volume. Filled symbols show soot particles with coatings added, open symbols show soot particles with coatings added and removed. The coating phase state during addition is indicated by the first (or single) capital letters S for solids and L for liquids. The coating phase during removal is indicated by the second capital letters. In our experiments, that DEC results in more complete compaction than CC (compare LL and LS). In Panel b, The shape factor of 1 for thick L (liquid) coatings and 1.2 for thick S (solid) coatings confirms that these two phases were liquid (spherical) and solid (aspherical), respectively. Fewer data points were available for solid coatings due to the experimental difficulty of adding solid coatings.

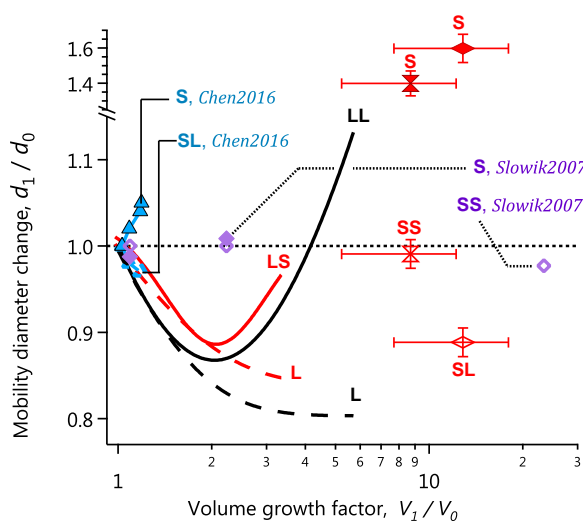


Figure 5. Same as Figure 4a but including data of Chen *et al.* (2016) (blue triangles) and Slowik *et al.* (2007) (purple diamonds), which are consistent with Path LS and Path SS of Figure 2, respectively. The coated data of Chen *et al.* (2016) indicate solid deposition, since mobility diameters increased upon coating. These three data sets are not plotted here in terms of shape factor χ (as in Figure 3b) because soot monomer and aggregate sizes differed between studies.

Supporting information for “Experimental compaction of soot aggregates by coating condensation and evaporation”

by Joel C. Corbin, Robin L. Modini, and Martin Gysel-Beer.

This Supplement contains additional discussion and figures related to the article.

S1 Mobility diameter and shape factor

The mobility diameter d_{mob} is given by (DeCarlo *et al.*, 2004),

$$\frac{d_{\text{mob}}}{C_c(\text{Kn}, d_{\text{mob}})} = \chi(\text{Kn}) \frac{d_e}{C_c(\text{Kn}, d_e)} \quad (\text{S1})$$

where the dynamic shape factor $\chi(\text{Kn})$ represents the ratio of the drag force on the particle to the drag force on its volume-equivalent sphere with diameter d_e , which is commonly obtained from single-particle mass (m_p) measurements via

$$m_p = \rho_p \frac{\pi}{6} d_e^3 \quad (\text{S2})$$

when the particle material density ρ_p is known (DeCarlo *et al.*, 2004). In Equation S1, the function $C_c(\text{Kn}, d)$ is the Cunningham slip correction, which accounts for the non-continuous nature of the gas-phase and which depends on the Knudsen number. In calculating the Cunningham slip correction C_c , we used the mean free path in air of 66.35 nm given by Jennings (1988). $\chi(\text{Kn})$ is a function of the Knudsen number ($\text{Kn} = 2\lambda/d$, where λ is the molecular mean free path of air and d is a particle diameter). For simplicity, we generally write χ for the transition-regime shape factor.

S2 Calculation of the phase diagram of anthracene

The phase diagram of anthracene was plotted using the Clausius-Clapeyron equation (Roux *et al.*, 2008),

$$\ln \frac{p_1}{p_2} = \frac{\Delta_x H}{R} \left(\frac{1}{T_2} - \frac{1}{T_1} \right) \quad (\text{S3})$$

where $\Delta_x H$ was either the enthalpy of vapourization $\Delta_{\text{vap}} H$ or sublimation $\Delta_{\text{sub}} H$. These were taken as 79.9 kJ/mol and 101.9 kJ/mol, respectively, following Roux *et al.* (2008). Note that $\Delta_{\text{sub}} H$ is equal to the sum of $\Delta_{\text{melting}} H$ and $\Delta_{\text{vap}} H$. Finally, R is the ideal gas constant.

The Clausius-Clapeyron equation requires knowledge of a reference vapour pressure, which we obtained using the Antoine equation $\log_{10} p = A - (B/(T + C))$, where p is the vapour pressure in bar at temperature T in Kelvin. We used $\{A, B, C\} = \{4.72997, 2759.53, -30.753\}$ from Burgess (2020) to estimate anthracene's vapour pressure at the bulk melting point of 489 K (216 °C). We then extrapolated this vapour pressure across the desired temperature range using the Clausius-Clapeyron equation and plotted the ratios of the calculated p . Though these coefficients are valid only down to 496.4 K (Burgess, 2020), our approach ensured overlap of the vapour pressures at the melting point. We did not find any literature values of p which resulted in a correct prediction of the melting point, which we attributed to the experimental difficulty in measuring the extremely low vapour pressures of solid anthracene (Roux *et al.*, 2008).

Reference: Donald R. Burgess, Jr. "Thermochemical Data" in NIST Chemistry WebBook, NIST Standard Reference Database Number 69, Eds. P.J. Linstrom and W.G. Mallard, National Institute of Standards and Technology, Gaithersburg MD, 20899, <https://doi.org/10.18434/T4D303>, (retrieved October 29, 2020).

S2

J.C. Corbin: Soot compacted by condensation or evaporation

S2.1 Phase diagram for designing restructuring experiments

Our anthracene experiments were designed based on the phase diagram shown in Figure S1a. The figure plots $S = p/p_0$, the saturation ratio with respect to liquid anthracene (Section 2), against temperature. By definition, $S = 1$ for bulk liquid anthracene, while $S < 1$ for capillary liquids due to their curvature. The figure illustrates capillary curvature for equivalent diameters of curvature > 2 nm (Ferry *et al.*, 2002). For solid anthracene, which exists only below the bulk melting point $T_{\text{melt, bulk}}$, $S < 1$ due to the greater order of the solid phase. $T_{\text{melt, bulk}}$ is illustrated by the vertical line at 488 K.

The anthracene phase diagram also includes a second vertical line to illustrate the melting point of nanoscale amounts of anthracene. This melting point, $T_{\text{melt, p}}$, is substantially lower than $T_{\text{melt, bulk}}$ due to the well-understood effects of melting-point depression (Pawlow, 1909; Schmidt *et al.*, 1998; Nanda, 2009; Christenson, 2001) which have even been specifically demonstrated in the context of soot compaction (Chen *et al.*, 2016).

The magnitude of nanoscale melting-point depression is quantified by the material constant β , which has been calculated as 1.303 for anthracene using molecular dynamics simulations (Chen *et al.*, 2014). The results of this prediction are shown by the upper axis of Figure S1a, which shows the size of a spherical particle with a melting point equal to the lower axis, $T_{\text{melt, p}}$. The melting point function $T_{\text{melt}}(m_p)$ increases asymptotically towards the bulk melting point (215 °C) with particle size. Particles with d_e greater than about 100 nm diameter have $T_{\text{melt}}(m_p)$ close to the bulk value, while small particles have much lower $T_{\text{melt}}(m_p)$. For example, $T_{\text{melt, p}} = 2$ nm is found at 348 K (75 °C), about 29% lower than the bulk melting point of $T_{\text{melt, bulk}} = 488$ K (215 °C). These values should be taken as qualitative, as the calculated $T_{\text{melt, p}}$ represents the equilibrium melting point; solids in confinement may remain liquid at even higher temperatures (Christenson, 2001). For example, Lopatkin *et al.* (1977) observed that anthracene films of thickness 10 nm to 16 μm form as liquids below 328 K. Nevertheless, these temperatures are comparable to our heater temperatures of 428–483 K, while some earlier work used lower temperatures (see Figures S7 and 5, and Section 4.3). Further details of $T_{\text{melt}}(m_p)$ and its calculation are given in Figure S7 and Section S4.

Figure S1b illustrates the use of this phase diagram to design the soot compaction experiments in Section 4. Each arc illustrates a process which we verified experimentally, primarily by measuring shape factors χ (Equation S1) as discussed below. The arcs illustrate capillary condensation at a single S (single pore size) for simplicity; in reality capillary adsorption would resemble an isotherm (e.g. Ferry *et al.*, 2002), though with relatively less adsorption than normal, since our experiments involved short timescales and therefore allowed less time for capillary condensation, t_c (Section 2). Note that, for simplicity, the arcs on Figure S1 do not emphasize the potential influence of freezing within capillary pores (Marcolli, 2014), which may lower S above the particle after freezing.

Each of the phase changes in Figure S1 may be experimentally achieved as follows. Liquid condensation or solid deposition may be achieved by passing soot particles through a heated reservoir of a given coating material, followed by a cooling section. The cooling section will produce a profile of supersaturation that is dependent on the temperature profile across the heated and cooling sections, which depends on flow rate, tubing material, and tubing insulation (Nguyen *et al.*, 1987). The rate of increase of supersaturation will dictate the amount of time available for heterogeneous nucleation of vapours onto the particles (discussed in Section 2). The maximum attained supersaturation will dictate the amount of coating condensed onto the sample particles. Condensation may occur via one of two processes, depending on the soot-coating contact angle θ and the supersaturation reached: it may form either menisci (first step of CC in Figure 1) or beads (first step of NDA in Figure 1) on the soot surface (Section 3). Competitive condensation to the walls of the system will also occur (Nguyen *et al.*, 1987).

Evaporation may be achieved by decreasing the saturation ratio of the aerosol. This may be achieved by removing vapours and is dramatically accelerated at elevated temperatures. For oleic acid coatings, where the melting point is above room temperature, evaporation is trivial and can be achieved with a catalytic stripper or thermodenuder. For anthracene coatings, the melting point is well above room temperature even after taking melting-point depression into account. Evaporation requires heating the anthracene coating above its melting point (≥ 80 °C) without allowing the coating to sublime. We achieved this by passing anthracene-coated soot through our second coating apparatus, while the second apparatus was heated to high temperatures and also filled with anthracene. The sample then follows the evaporation curve in Figure S1 (thin blue solid line). Our apparatus was only able to sustain these conditions for a short period, before the anthracene in apparatus 2 was ‘distilled’ from the heating section to the cooler tubing downstream by sublimation-deposition.

When the second apparatus was depleted of anthracene, the sample followed the sublimation curve in Figure S1 (thin red line). Sublimation was also achieved by heating anthracene in the catalytic stripper and thermodenuder.

Thus, by combining the experimental conditions required to achieve each phase change, the four restructuring pathways in Table 1 may be achieved. To summarize, we achieved Path **LL** using oleic acid, and Paths **LS**, **SS**, and **SL** using anthracene. We achieved Path **LL** under

conditions where capillary condensation was possible, but not under conditions where NDA was possible (Figure 1). The NDA mechanism has been achieved previously by others ((Ma *et al.*, 2013a; Chen *et al.*, 2018)) as discussed in Section 3.

S3 Additional Experimental Methods

S3.1 Soot samples

Soot was generated by a miniCAST 5201c soot generator (Jing Ltd., Switzerland) which consists of a partially-quenched propane diffusion flame. The miniCAST was operated under lean combustion combustions, with the following settings for each {gas, flow in mL min⁻¹}: {propane, 60}, {premixed nitrogen, 0}, {combustion air, 1550}, {dilution air, 2e4}. Premixed nitrogen refers to potential premixing with combustion air. We avoid using the CAST burner to produce so-called “low-BC fraction” soot, which is quenched earlier in the combustion process to produce incompletely-graphitized particles that are poor surrogates for atmospheric soot (Maricq, 2014). A 1.5 m³ steel tank was used as a reservoir during the experiments.

S3.2 Real-time measurements

As depicted in Figure S2, a number of instruments were used to characterize the soot samples in real time. The total flow was 0.71 min⁻¹. A first Differential Mobility Analyzer (DMA1, built at PSI, with similar dimensions to the Model 3801 DMA of TSI Inc., USA) pre-selected particles, typically at 300 nm. The resulting monodisperse aerosol was either sampled directly or processed as described below.

The aerosol was measured by a Scanning Mobility Particle Sizer (SMPS; comprised of a similar DMA, DMA2, plus a TSI 3022a Condensation Particle Counter, CPC), scanning from 100 to 700 nm. In some cases, we bypassed DMA2 in order to test whether new particles (with diameter <100 nm) were forming in the coating apparatus; such conditions were always avoided. In parallel, a Single Particle Soot Photometer (SP2; Schwarz *et al.*, 2006; Laborde *et al.*, 2012) simultaneously measured single-particle BC mass m_{BC} by laser-induced incandescence and optical size by light scattering. The SP2 was frequently operated behind an Aerosol Particle Mass analyzer (APM; Model 3601, Kanomax Japan), which classifies particles by their mass-to-charge ratio m/q . Using custom software written in LabView, the APM was scanned through m/q settings while the SP2 was used to selectively count singly charged ($q = 1$) BC particles exiting the APM. Like a high-resolution optical particle counter, the SP2 is able to discriminate singly charged particles because its signals are proportional to particle mass, which reduces ambiguity in the data relative to APM-CPC measurements. The modes of the resulting mass distributions were fitted by lognormal or asymmetric normal curves (Tajima *et al.*, 2011) and used to define the total particle mass. The measured total mass was used to calculate coating volumes as described in the manuscript.

S3.3 Offline measurements

TEM was performed with a JEOL 2010 at 200 keV after electrophoretic sampling particles onto 300-mesh copper grids with a 1-2 nm amorphous carbon film. The copper grids were obtained from Quantifoil (Großlöbichau, Germany).

Sampling was performed using a Partector (Naneos GmbH, Windisch, Switzerland), which charges particles with a corona charger before electrophoretic sampling. TEM samples were performed for the maximum coating volumes (maximum V_1/V_0).

S3.4 Soot coating addition and removal

Soot coatings were added using one of two apparatuses. The first was similar to that described by Moteki and Kondo (2007) and was constructed at PSI by M. Heringa. It consisted of two concentric stainless steel tubes (12 mm and 8 mm). Aerosol samples flowed in through the outer tube and out through the inner tube. The outer tube was terminated at one end by a stainless steel cap, which was filled with either oleic acid or anthracene crystals. The cap was placed on a hot plate and heated to saturate the aerosol flow. The second apparatus consisted of a simple copper tube wrapped first in heating tape, then in ice–water packs and was similar to that described by (Nguyen *et al.*, 1987). Coating materials were placed in a bend in the copper tube. The second apparatus was able to reach higher coating thicknesses due to the active cooling stage and the high thermal conductivity of copper. The second apparatus was also necessary for the anthracene evaporation experiments described in Section 4.1.

The coating apparatuses were operated at different temperatures for oleic acid (90 %, Sigma-Aldrich) and anthracene (99 %, Sigma-Aldrich). For oleic acid condensation, the heater was operated between 94 and 140 °C. Above 140 °C new-particle formation occurred, indicating

S4

J.C. Corbin: Soot compacted by condensation or evaporation

that excessive supersaturations were being reached after the coating apparatus. Anthracene coatings were obtained with a heater temperature of 95–202 °C. Above 202 °C, the reservoir emptied too quickly for the measurements. Note that the thermocouple was placed between the heating plate and the sample, so the reported temperatures are upper limits. The lower half of the apparatus was insulated and the upper half cooled by room air to maximize the achieved supersaturations. For some anthracene experiments, even higher supersaturations were achieved by immersing the lower third of the apparatus in oil. The oleic acid experiments lasted one day and were performed in sequence: the highest temperatures were used last. Afterwards, the oleic acid was observed to have transformed from a light-yellow to a reddish-brown liquid, indicating that a chemical transformation had taken place. However, our results are consistent with previous work (Ghazi and Olfert, 2013) and indicate that this change had a negligible effect on the density of the oleic acid which was taken as 895 kg m³ in our calculations.

The anthracene experiments lasted three days in total and were not performed in sequence. The maximum temperature used was 202 °C. In the early minutes of some high-temperature anthracene experiments, the SMPS appeared to measure the tail of a nucleation mode. As no difference in the results was observed when this mode was present, we conclude that it did not influence the experiments.

The primary denuder used in this work was a catalytic stripper (CS015, Catalytic Instruments GmbH, Rosenheim, Germany), which vapourizes and then oxidizes organic molecules at 350 °C. In some experiments, this stripper was replaced with the activated-charcoal thermodenuder described by Burtscher *et al.* (2001), so that the additional experiments where soot was pre-denuded prior to coating could be performed. In those experiments, described in Section 4.2.3 in the manuscript, we pre-denuded soot at 350 °C using the thermodenuder before coating particles as usual and denuding particles with the catalytic stripper, at 350 °C to 200 °C and 150 °C. For all stripper temperatures, the original particle mass (mean ± standard deviation 6.40 ± 0.15 fg) was measured as returning to its original value, within uncertainty (6.38 ± 0.18 fg).

S4 Melting-point depression: further discussion and calculations

Physically, melting point depression may be alternatively viewed as a reduction of intermolecular forces due to the disorder of nanoscopic quantities of anthracene (Aubin and Abbatt, 2006) or as the result of balancing bulk and surface energy terms (Christenson, 2001). The magnitude of melting-point depression for anthracene was estimated for Figure S7 using a size-dependent thermodynamic model of nanoscopic melting-point depression (Nanda, 2009):

$$\frac{T_{m, \text{particle}}}{T_{m, \text{bulk}}} = 1 - \left(\frac{\beta}{d_e} \right) \quad (\text{S4})$$

where $T_{m, \text{particle}}$ is the melting point of a particle with spherical-equivalent diameter d_e and $T_{m, \text{bulk}}$ is the melting point of bulk material ($d_e > 100$ nm, see Figure S7). This model has been validated experimentally (Nanda, 2009) and is valid for materials which melt homogeneously or from the surface inwards. Using a molecular-dynamics model, Chen *et al.* (2014) found that pyrene melts via both of these mechanisms (Chen *et al.*, 2014) and estimated the material-specific parameter β as 1.303 for pyrene (four compact aromatic rings) and 1.312 for coronene (seven compact rings). As these two values are virtually identical we have used $1.3 \pm 25\%$ for anthracene (three linear rings) in Figure S7. This β results in a melting point for 1 nm spheres which is about 2/3 of the melting point of bulk anthracene, which is close to the melting point depression measured experimentally by Lopatkin *et al.* (1977) for anthracene thin films. This consistency is in line with expectations, since β is a thermodynamic parameter, a function of the solid density, liquid density, surface energies of the solid–vapour and liquid–vapour interfaces, and the bulk latent heat of fusion (Nanda, 2009).

We note that our use of Equation S4 is different to that of Chen *et al.* (2016), who were the first to consider the effects of melting-point depression on soot restructuring. Those authors considered thin-film thicknesses when applying Equation S4, whereas we have considered equivalent spheres ($d_{\text{sph-equiv}}$). They observed PAH restructuring at equivalent film thicknesses (calculated from single-particle mass measurements) of 0.2 nm, which is half the 0.4 nm thickness of a graphene sheet (Nemes-Incze *et al.*, 2008). They therefore argued that their observations demonstrated capillary condensation and restructuring, in agreement with the conclusions of the present work..

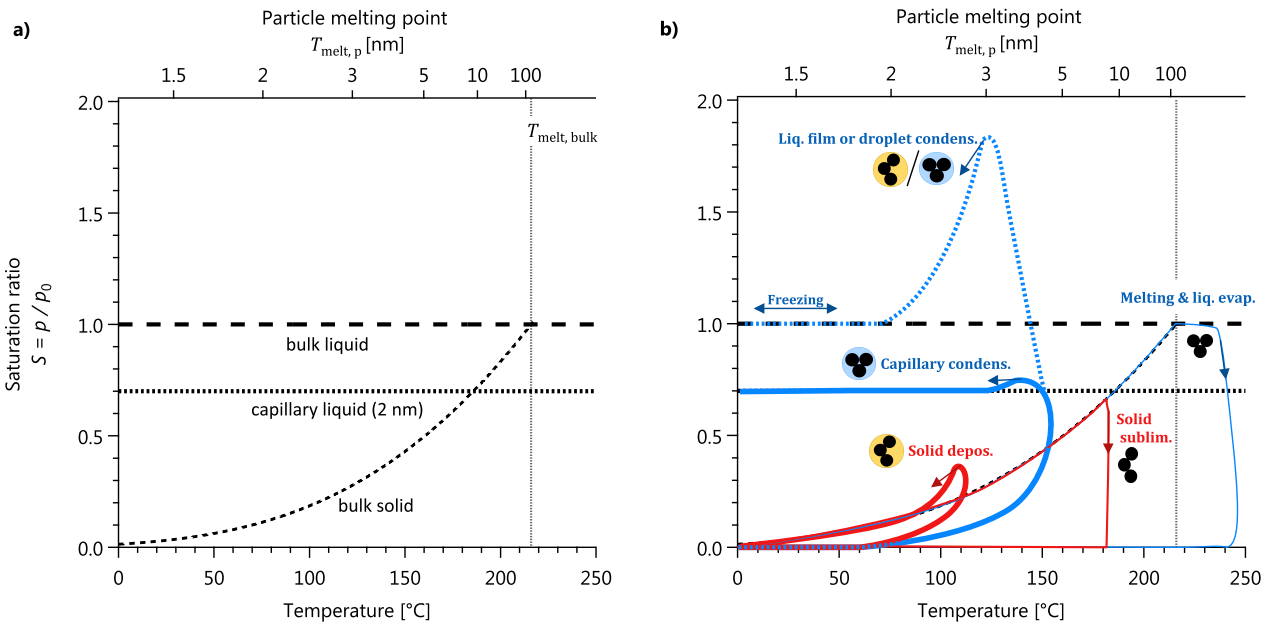


Figure S1. Equilibrium phase diagram for anthracene, as used to design the experiments shown in Figure 2. Saturation ratios are plotted with respect to the bulk liquid vapour pressure, p_0 . Panel **a** shows the equilibrium saturation ratios S for bulk solids, bulk liquids, capillary liquids with > 2 nm equivalent diameters and the melting-point depression associated with nanoscopic quantities of material (Section S2.1). Nanoscopic quantities of material are expressed in equivalent nanoparticle diameters on the top axes. Panel **b** qualitatively illustrates the experimental pathways used to add (thick lines) or remove (thin lines) coatings. Coatings are either solid (red) or liquid (blue) phase at the time of removal; line thicknesses are varied so that the different pathways can be distinguished visually. By combining one addition and one removal pathway, different compaction endpoints can be achieved, as shown by the particles. Note that the depicted maximum supersaturations are conservative; some laboratory studies have used $S > 20$.

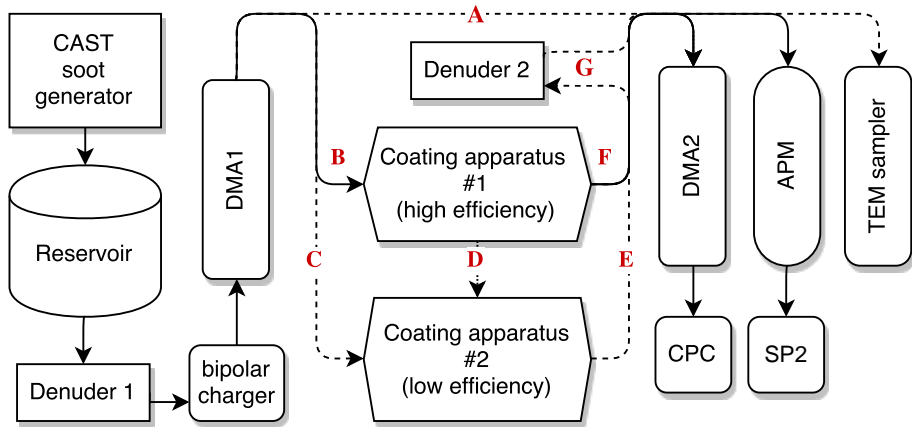


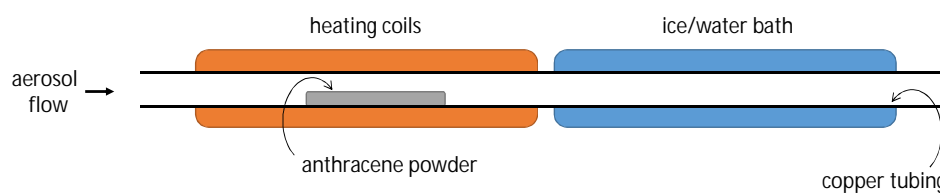
Figure S2. Experimental setup used to process soot particles through the different pathways given in Table 1 and related Figure 2. Details of the coating apparatuses are illustrated in Figure S3. Pathways were achieved as follows. Path (LL): route CEG with oleic acid; Path (LS): route CEG with anthracene; Path (SS): route BFG with anthracene; Path (SL): route BDE with anthracene and anthracene-saturated walls in the second coating apparatus. Reference untreated samples were measured through line A. The denuder G was removed to measure coated particles. Dashed lines indicate temporary connections. The SP2 was used to differentiate particle charges only, not to measure single-particle mass.

S5 Supplementary figures

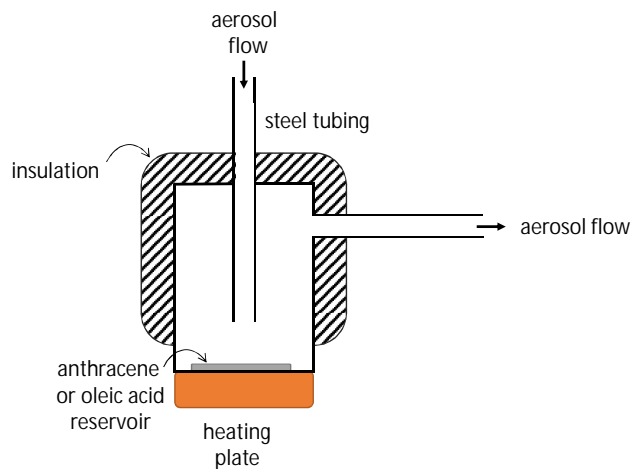
S6

J.C. Corbin: Soot compacted by condensation or evaporation

Coating apparatus #1



Coating apparatus #2

**Figure S3.** Schematic of the (a) high-efficiency copper coating apparatus #1 and (b) low-efficiency steel coating apparatus #2.

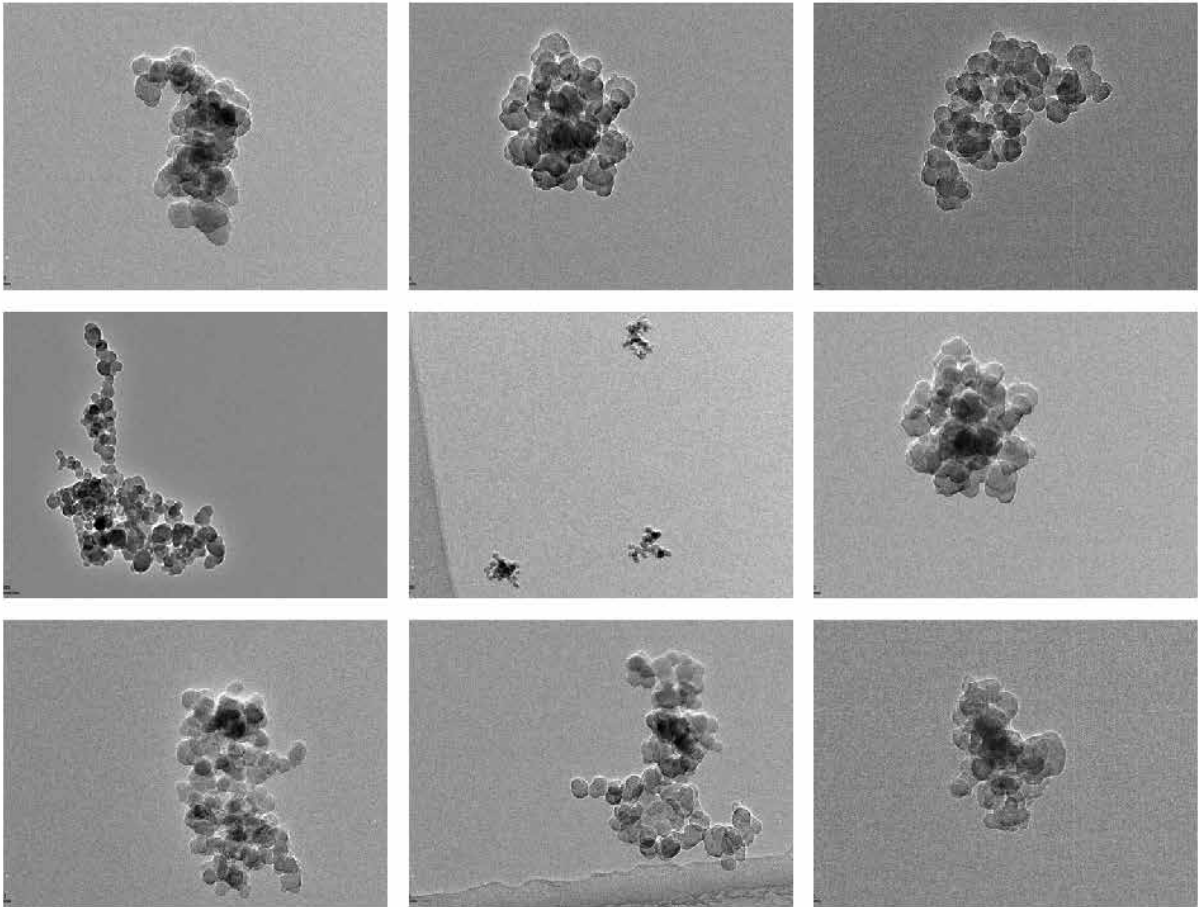


Figure S4. TEM images of 300 nm soot after anthracene coating ($m_1/m_0 = 2.6$) and denuding via Path **LS** of Figure 2. Scale bars are omitted since all soot was composed of monomers with 30 nm diameter (Figure S8).

S8

J.C. Corbin: Soot compacted by condensation or evaporation

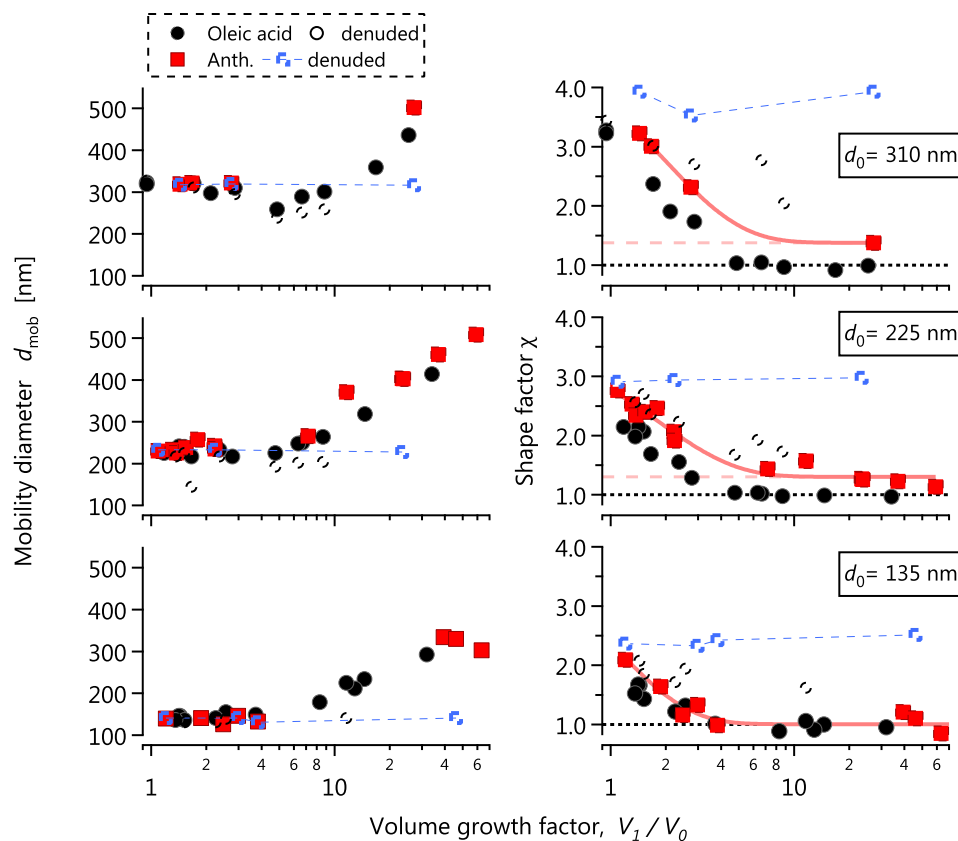


Figure S5. Data from Slowik *et al.* (2007), reanalyzed to illustrate coating/denuding without a change in the final d_{mob} or χ . Initial particle diameters are 135, 225, and 310 nm. This demonstrates deposition/sublimation of anthracene (Path SS in Figure 2). Left and right panels show mobility diameter and shape factor χ as a function of coating volume. Circles reflect oleic acid condensation, squares anthracene deposition. Since $\chi \approx 1$ at large V_1/V_0 for both substances, anthracene likely condensed as a supercooled liquid. The fits on the right hand side reach a minimum of $\chi = 1.37, 1.3$, and 1.0 for the 310, 225, and 135 nm particles, respectively.



Figure S6. Photograph of a spatula upon which anthracene was deposited in our coating apparatus. The crystalline structure of the deposit is clearly visible. The conditions used for this experiment were used for the experiment labelled Path **SS** in Figure 2.

S10

J.C. Corbin: Soot compacted by condensation or evaporation

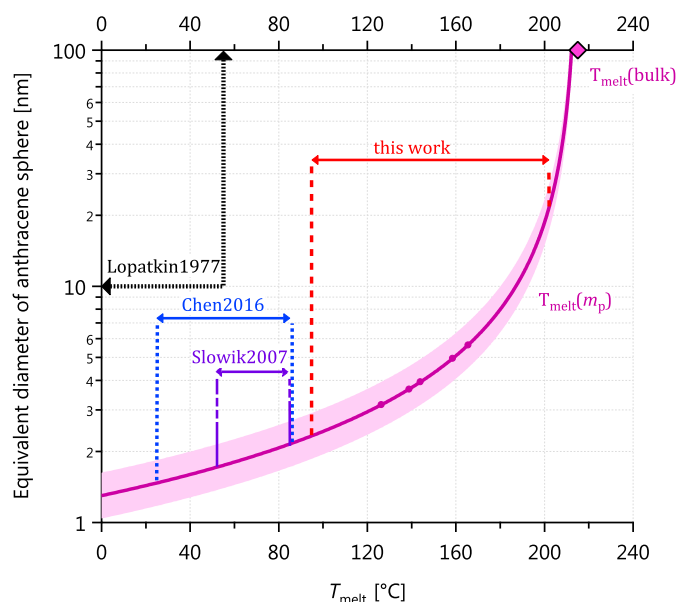


Figure S7. Melting point depression of nanoscopic quantities of anthracene, as discussed in the text. Overlaid are the temperatures at which these and related anthracene experiments have been carried out. The curve indicates the melting point depression for nanoscopic quantities of anthracene based on molecular dynamics simulations at the points marked with spheres (Chen *et al.*, 2014). The asymptote of this curve is the melting point of bulk anthracene (216 °C, ♦). The studies of Chen *et al.* (2016) and Slowik *et al.* (2007) are similar to ours and discussed in Section 4.3; the study by (Lopatkin *et al.*, 1977) showed that anthracene thin films (thickness 10 nm to 16 μm) form as liquids below 55 °C.

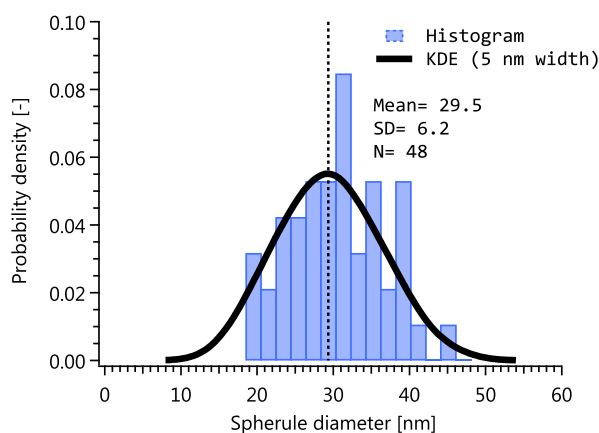


Figure S8. CAST Soot spherule diameters, measured manually from the TEM images. KDE is the kernel density estimated with a Gaussian kernel.